TAMPEREEN TEKNILLINEN YLIOPISTO
TAMPERE UNIVERSITY OF TECHNOLOGY

YOUSOF MARDOUKHI

CHARGE DENSITY CONTROL OF QUANTUM DOT LATTICES

Master of Science thesis

Examiner: Prof. Esa Räsänen
Examiner and topic approved by the
Faculty Council of the Faculty of
Natural Sciences
on 4th February 2015

ABSTRACT

YOUSOF MARDOUKHI: Charge Density Control of Quantum Dot Lattices
Tampere University of Technology
Master of Science thesis, 74 pages, 7 Appendix pages
18 February 2015
Master's Degree Programme in Science and Bioengineering
Major: Nanotechnology
Examiner: Prof. Esa Räsänen
Keywords: Cellular automata, Quantum dots, Quantum optimal control theory, Quantum dot cellular automata

The complexity of physical systems in nature is an obstacle for human desire and curiosity to explore new realms of knowledge. As we go further and further, more powerful computers with higher capability both in processing and storing of information are needed. According to Moore's law, the computational power of devices grows exponentially, meanwhile their size decreases at the same rate. But at this very moment, this trend is getting saturated and a new jump into a new scale cannot be avoided. Devices manufactured with smaller size exhibit quantum mechanical behaviour. Due to the intrinsic uncertainty which quantum mechanics has, the behaviour of these systems must be controlled with great precision.

Deterministic logical computations cannot be done by these devices, since logical operations need to have well-defined sets of input. This is a crucial concern especially if the set of inputs corresponds to the states of quantum mechanical systems. Quantum optimal control theory lets us identify the constraints one has to consider for the sake of the desired manipulation of quantum mechanical systems.

The aim of this project is to put the very first stone toward exploiting the controllability of quantum dot cellular automata which are among the candidates for the next generation of transistors as building blocks of logical circuits.

PREFACE

I am so grateful to those who have given me this opportunity to satisfy my desire of doing scientific work. I am thankful to my adviser, Prof. Esa Räsänen who has given me courage and support in doing this project.

It is a valuable fortune to be in a group which provided a warm and friendly atmosphere. I would like to thank my colleague, Nikolay Shvetsov-Shilovskiy for his always warm discussion attitude and his wife, Liza Shvetsov-Shilovskiy for her kindness and her hospitality. I am also warmly thankful to Alexander Odriazola and Janne Solanpää.

I wish to thank Prof. Stephan Foldes, Prof. Tapio Rantala and Dr. Jae-Hyung Jeon for letting me to be involved in their scientific works. They have given me an invaluable opportunity to explore new ideas and tackle new challenges in the fields of mathematics and physics.

I owe boundlessly to my mother and my father, who devoted their lives and souls for giving me life where I could follow my own path. And my brother Ahmad who always supports me with no expectation. Also I want to thank my friend Ayat and his wife Niloofar, for their indispensable friendship and the countless memories which I have with them and their support during my studies in Finland.

My last special gratitude goes to my girlfriend Aleena, who stands firm beside me in my both happinesses and sadnesses, and her persuasion and encouragement which give me confidence in setting my feet. For her unconditional support and above all, for her true love.

Tampere, 18.2.2013

Yousof Mardoukhi

TABLE OF CONTENTS

LIST OF FIGURES

LIST OF TABLES

LIST OF ABBREVIATIONS AND SYMBOLS

2DEG	Two-dimensional electron gas
AND	AND gate
CA	Cellular automaton (automata)
CNOT	Controlled-NOT gate
DQD	Double quantum dot
EPR	Einstein-Podolsky-Rosen
FET	Field-effect transistor
MPS	Matrix-product state
OBC	Open boundary condition
OCT	Optimal control theory
QCA	Quantum dot cellular automaton (automata)
QD	Quantum dot
QOCT	Quantum optimal control theory
SD	Schmidt decomposition
SVD	Singular-value decomposition

$\mathbb{1}$	Identity operator
$\otimes_2$	Addition modulo 2
∇	Del operator
A	Field amplitude, matrices of a matrix-product state
$\mathcal{A}$	Contraction map in matrix-product state representation
a_0	Bohr radius
C	Capacitance
D	Bond dimension
$\mathbb{C}$	Set of complex numbers
E	Electrostatic coupling energy in double quantum dots
E_h	Hartree energy
$\mathcal{E}$	Ground state energy of a quantum dot
e	Elementary charge (negative)
H	Hadamard gate
$\mathcal{H}$	Hamiltonian
$\hbar$	Reduced Planck constant
Im	Imaginary part
J	Lagrange functional
k_B	Boltzmann constant
$\mathcal{L}$	Discrete cellular state space

N	Number of cells in a one-dimensional cellular automata, number of electrons in a quantum dot
$\mathcal{N}$	Set of neighbouring cells in cellular automata
$\hat{O}$	Target operator
$\mathcal{O}$	Error order
$\hat{\mathcal{P}}$	Momentum operator
R	Electrical resistance
r	Neighbourhood range in cellular automata, position vector
T	Absolute temperature, pulse duration
$\hat{\mathcal{T}}$	Kinetic energy operator
t	Time
U	Electrostatic energy of a quantum dot, gate voltage
$\mathcal{U}$	Dyson operator
V_c	Confinement potential
V_d	Drain voltage
V_g	Gate voltage
V_s	Source voltage
$\hat{\mathcal{V}}_0$	Stationary potential operator
X	NOT gate
$\mathbb{Z}_k$	Integers modulo k
α	Probability amplitude, truncated basis in matrix-product state representation
β	Probability amplitude, multiplier in the spatial Gaussian profile of the voltage gate
β_{00}	Bell state
β_{01}	Bell state
β_{10}	Bell state
β_{11}	Bell state
Γ	Unitary matrices of singular value decomposition
γ	Arbitrary phase in a wave function
Δ	Energy difference between the bonding and antibonding states in double quantum dots
Δt	Increments for time step
Δx	Increments for real-space step
δ	Dirac delta-function, Kronecker delta
ϵ	Ground state energy
Θ	Heaviside distribution function
θ	Polar angle
Λ	Singular value matrix

λ	Langton parameter, singular value in singular value decomposition
μ	Chemical energy
μ_d	Drain chemical energy
μ_s	Source chemical energy
π	Number pi
ρ	Density matrix (density distribution)
Σ	Local value space, summation symbol
σ	State of a cell in cellular automata, variance of a Gaussian distribution
σ_x	x-Pauli matrix
σ_z	z-Pauli matrix
Φ	Eigenvector of a reduced density matrix
ϕ	Transitional rule, azimuthal angle
χ	Lagrange multiplier, measure of entanglement
Ψ	Wane function
ψ	Wave function
Ω	Effective resonance frequency between the bonding and antibonding states in a double quantum dot
ω	Frequency of initial fields in optimal control theory procedures
ω_{th}	Threshold frequency

1. INTRODUCTION

Demands for more powerful hardware resources for computational purposes grow exponentially. As a recent example, a hydrodynamic study of the galaxies properties carried out by Vogelsberger *et al.* [1], costed 19 million CPU hours and 8192 CPUs. The enormous amount of computational time spent for this simulation show the need for urgent developments in hardware technology.

This observation and the trend which Gordon Moore predicted [2] cause an unavoidable transition in the designation of electrical circuits and fabrication of new materials in order to provide a fast switching time and low energy consumption. Besides, the volume which the device occupies is a critical consideration one has to bear in mind.

Among many new developments in the construction of nano-electrical devices and materials such as Josephson computers, graphene and nanotubes, one specific nanodevice called quantum dot cellular automaton, is of popular interest. An essential reason that makes this device worth studying is the fact that cellular automata are extensively used for the study of complex systems, and besides that, their presence in the studies of logical circuits is indisputable.

Many studies have been carried out on quantum dot cellular automata, both on their architectural structures and logical properties. Quantum dot cellular automata, although they correspond to the classical interpretation of cellular automata, have quantum mechanical behaviour within their nature. Hence, for deterministic computational purposes, the quantum mechanical nature of quantum dots must be tamed.

The objective of this thesis is to study and exploit whether a quantum dot cellular automata can be controlled by an external agent, in this study by a local voltage gate. Among many existing methods for control problems, the mathematical tool used here is quantum optimal control theory. We seek for specific properties of an electric field to transfer the initial state of the quantum dot cellular automata to a final desirable one.

After providing some introductory concepts such as cellular automata and quantum

dots, the mathematical framework of the study is explained. This is followed by the main results and conclusions.

2. CELLULAR AUTOMATA

Cellular automata (CA) are tightly akin to the concept of complex systems. Generally speaking, a complex system is a dynamical system which exhibits non-linear behaviour. CA are mathematically found to be the simplest representation of large a class of complex systems. The concept was first coined out by Stanislaw Ulam and John von Neumann. Historically, the automaton which von Neumann modelled [3], was the first discrete parallel computational model which has been shown to be a universal computer [4]. CA are found to be powerful idealisations for a variety of systems and phenomena ranging from fluid flow to processor architectures, cryptography and also to pattern formation.

CA belong to the class of discrete and deterministic mathematical systems, both spatially and temporally. CA are grid lattices where each cell evolves through discrete time steps. In general, if a special modelling is not required, most CA have five common characteristics:

- They have an underlying structure called a *lattice*. The lattice consists of cells which are arranged according to specific symmetries of the lattice.
- CA are homogeneous, meaning that there is no preference between cells.
- Each cell has a state, which belongs to the set of allowed states.
- The cell can only interact with its neighbouring cells. At any instance the state of the cell updates by the transition rule accordingly.
- The transition rule for a specific cell only depends on its state and the state of its neighbouring cells.

CA with only these simple characteristics are capable of producing global order and correlation, although the interactions are local.

Three specific properties which can be considered as crucial characteristics of such an automaton are that firstly, they are spatially and temporally discrete: They consist

of a denumerable units called *cells*, which at each time unit a cell can possess a value belonging to the set of allowed states. At the next time step the cell interacts with its neighbours and updates its state according to the set of rules. Secondly, these machines are *abstract*. They have purely mathematical representations giving them the ability to be implemented in fields ranging from mathematical logic to a vast area of physical structures. And lastly, they are *computational* systems. With a suitable choice transition rules, CA become universal Turing machines [5, 6], and therefore they are able to perform computations. Yet another feature of CA is their capability of performing computations in a *parallel* fashion. As mentioned, the areas of applicability of CA are broad, but they can be entitled under four main categories:

1. Powerful computational machines,
2. Discrete dynamical simulations,
3. Pattern formation and complexity behavioural studies,
4. Fundamental physics.

The first area emphasises the previously mentioned Turing-like machine capability. The second area exploits the strength of CA in modelling and solving particular problems. Successful and interesting examples are Ising models [7], neural networks [8], and turbulence phenomena [9]. By imposing local interactions and conservation laws of physics, this simple abstract modelling of CA exactly reproduces macroscale behaviour of the continuum system. Even recently, cellular automata have been used to study cancer growth, propagation of cracks in solid materials, or detection of grain boundaries in inhomogeneous materials [10–13].

The last two areas enter into more philosophical aspects of the CA description. One of the most prominent study in the realm of complexity was ignited by the introduction to the famous *Conway's game of life* [6], and later by the study of Dennett on deterministic formation of patterns based on this automaton [14]. Also a discrete representation of quantum field theory by the means of CA arouses the idea that nature itself may be represented by CA (see Ref. [15]).

Through this chapter, a brief definition of complex systems, a mathematical definition of cellular automata, and their classification and applications are given. Although the definition covers all the classes of the CA, the emphasis in the following sections is particularly on two-dimensional CA and on their different variations.

2.1 Cellular automata description

Although there are many varieties of CA, each one is particularly defined to meet the requirements of a specific model. They have four generic characteristics in common:

Discrete cellular state space denoted by $\mathcal{L}$, is a discrete arrangement of cells attached to the discrete lattice structure. The dynamics and the evolution of the system take place in this space. $\mathcal{L}$ has the dimension of the lattice structure which means that it can be generally an n-dimensional space.

Local value space Σ is the set of allowed states; each cell can possess at time step t a certain state which belongs to Σ:

$$\sigma_{i\in\mathcal{L}}(t) \in \Sigma \equiv \{0, 1, 2, ..., k-1\}. \tag{2.1}$$

Here σ_i is the value of the cell indexed with i, where indexing of the cells is typically based on the symmetry groups of $\mathcal{L}$. The restriction on the set Σ is the fact that it has to be a finite commutative ring (the binary operation has to be understood from the context). Usually the choice of such a set is $\mathbb{Z}_k$ (*integers modulo* k). This characteristic is among the properties which differentiates between the classical CA and quantum CA (not to be confused with quantum-dot cellular automata). In the classical CA, the state of the cell can be assigned only to one of the allowed states in set Σ, while in quantum interpretation, the cell can be in a superposition state of the allowed states.

Boundary conditions inevitably change the dynamics of the CA and, in consequence, a pattern produced by the system. Typically a *periodic boundary condition* is a common choice. Sometimes, to decouple the dynamics of the boundary cells from the rest, they are set to predefined states.

Transitional rule, commonly denoted by ϕ, is defined by any map from $\Sigma^n \to \Sigma$ where n denotes the number of nearest neighbours that affect the state of a given cell (notation Σ^n is equivalent to the Cartesian product $\underbrace{\Sigma \times \Sigma \times ...\Sigma}_{n}$). Denoting the set of all neighbour cells of the cell i by $\mathcal{N}_i$ (also $i \in \mathcal{N}_i$), the transition rule is defined as

$$\sigma_i(t+1) = \phi\Big(\sigma_j(t) \mid j \in \mathcal{N}_i\Big). \tag{2.2}$$

One time step iteration corresponds to the update of all the cells in $\mathcal{L}$ after a simultaneous application of the transition rule ϕ.

2.1.1 One-dimensional cellular automata

In a one-dimensional CA, the set $\mathcal{L}$ corresponds to a line of cells (finite or infinite set). The radius of the neighbourhood determines the range of the interaction and it is denoted by r. The range determines the index of the furthest cells which belong to the set $\mathcal{N}_i$. Therefore, the index of the neighbours of the cell i belongs to the interval $[i-r, i+r]$ (it has to be noted that this interval is defined on the set of integers) (Fig. 2.1). Therefore for a *range-r* one-dimensional CA, the transitional function ϕ has $2r+1$ inputs and it is written as follows:

$$\sigma_i(t+1) = \phi(\sigma_{i-r}(t), ..., \sigma_i(t), ..., \sigma_{i+r}(t)). \tag{2.3}$$

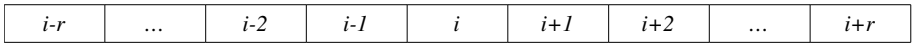

Figure 2.1 *One-dimensional range-r CA.*

There are k^{2r+1} possible inputs for the function ϕ where k is the cardinality of the set of allowed states Σ. The exponential growth in the number of possible inputs is one of the most important features of CA in cryptography. This representation is in a one-to-one correspondence with the string representation of the elements of the set of all polynomials with degree $2r+1$ over a finite k-element field [16]. Hence, the set of all one-dimensional CA, where the range belongs to the set of natural numbers, form a ring of polynomials over a k-element field. Thus, by taking a quotient set with respect to a prime element of the ring of polynomials, a new finite field can be constructed in order to embed the key for cryptological purposes. For a clarification of how a CA evolves, consider the case in which the underlying field is a two-element field ($\Sigma = \{0, 1\}$ with the binary operation addition *modulo* 2) and $r = 1$. The possible local interactions depend on the states of the three adjacent cells. Thus, there are eight different states and a possible transition is given in the figure below.

111	110	101	100	011	010	001	000
0	1	0	1	1	0	1	0

Figure 2.2 *One-dimensional CA with two-element underlying field. The transition function* $\phi(\sigma_{i-1}, \sigma_i, \sigma_{i+1}) = \sigma_{i-1} \oplus_2 \sigma_{i+1}$ *governs the evolution of the CA.*

One way of addressing the transition rule instead of providing its catalogue for $k = 2$ and $r = 1$, is to associate a *number* to each specific rule. There are eight possible binary states in total for three adjacent cells ($2 \times 2 \times 2 = 8$). Therefore, there are $2^8 = 256$ different elementary transition rules which can be represented by a binary string of length eight. As an instance, for the table above, the second row shows how the transition is done and can be represented by the string (01011010_2) which equals 90 in decimal. In this way, one can search through the database (already available online) for the pattern which is produced by a specific rule and the given initial condition [17].

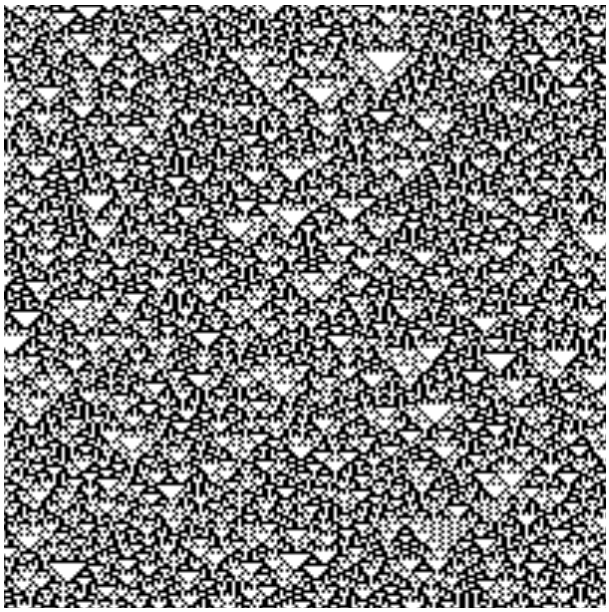

Figure 2.3 *Chaotic pattern generated by the rule 90 CA. This rule belongs to the class of chaotic CA. This pattern shows how, from a deterministic rule, global chaotic behaviour emerges. This clearly demonstrates that global complex behaviour is not necessarily a consequence of underlying complex interactions. In contrast, such emergent global patterns can be generated by simple local interactions.*

Since the underlying field resembles a Boolean ring, the above catalogue is commonly called the *truth table* of the transition function ϕ. The temporal state of the CA cells is given by a simultaneous application of ϕ to each cell. The first five temporal states of a CA with $N = 10$ and the cells initiated in the state $\sigma(t = 0) = (0100011010)$, and periodic boundary conditions, is given in Fig. 2.4.

Depending on the properties of the transition rules, CA can be categorised based on

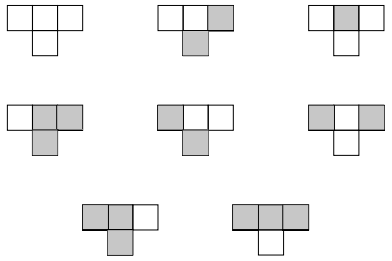

time(step)	$\sigma(t)$
0	0 1 0 0 0 1 1 0 1 0
1	1 0 1 0 1 1 1 0 0 1
2	1 0 0 0 1 0 1 1 1 1
3	1 1 0 1 0 0 1 0 0 0
4	1 1 0 0 1 1 0 1 0 1
5	0 1 1 1 1 1 0 0 0 1

Figure 2.4 *Left: it is convenient for $r = 1$ to represent the transition rules by T-Polyominos [18]. Here, the states '0' and '1' are shown by squares filled with grey and white colours, respectively. Right: evolution of a CA with $N = 10$ and $r = 1$. The states are updated at each iteration simultaneously by the application of the transition rule ϕ.*

their dynamics evolution. CA with simple rules usually have steady-state behaviour or may have dynamics with limit cycles, but in case of complex transitional rule, it may occur that the CA behave chaotically (there are two classes of automata in which their transition is either deterministic or indeterministic. Here we do not deal with indeterministic CA; therefore the chaotic behaviour is due to deterministic rules). It is not possible to determine these classes analytically. The classification is done based on extensive simulations on one-dimensional CA with different initial conditions, neighbourhood ranges and transition rules. The simulations have showed that the pattern generated by the evolution of a CA belongs to one of the four classes listed below:

1. The pattern is homogeneous. All the cells attain either the state '0' or '1'.
2. The pattern flows in a stable steady-state fashion or evolves periodically.
3. The behaviour of the CA becomes chaotic.
4. The evolution leads to the formation of complex localised structures propagating through each iteration.

The behaviour of the fourth class lies between chaotic and periodic patterns. This class is tightly connected to the *phase transition* phenomenon in physical systems. Thus, it is vital to identify the rules for which the behaviour of the CA resembles a phase transition. The rule 54 produces some patterns which flow through the evolution of the CA and remain unchanged. They are called *solitons*. Although there are some features which exhibit chaotic-like behaviour, they are not as chaotic as patterns generated by the rule 105. The solitions are *particle-like* patterns which *encode* the information inside themselves. Since their shape is persistent through the evolution of the system, somehow it can be interpreted that these patterns are the

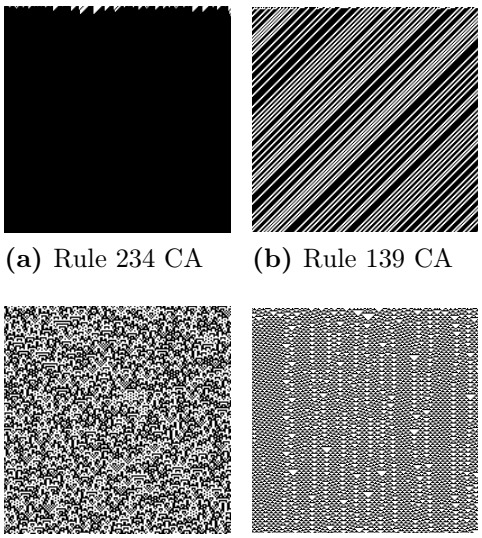

(a) Rule 234 CA **(b)** Rule 139 CA

(c) Rule 105 CA **(d)** Rule 54 CA

Figure 2.5 *(a) Cellular automaton belongs to the homogeneous class. (b) Stable steady-state cellular automaton with a periodic pattern. (c) A cellular automaton with chaotic behaviour. In this class, there is no flow of information and it corresponds to the maximal loss of information. (d) A cellular automaton with complex behaviour. The flow of local structures (solitons) is evident in the figure; these kinds of cellular automata are capable to encode information.*

agents for the flow of information. This feature is important especially in coding and information theory. The periodic behaviour in encoding of an arbitrary information makes them vulnerable to be exploited by trivial decoding algorithms. Also periodic patterns due to their simple nature are not capable to store a considerable amount of information.

Therefore, based on the above statements, the capability of a CA on performing computations depends on its ability to produce such solitons. This solely depends on the underlying rule [19]. More interestingly, the rules which belong to the fourth class are the only ones which can emulate the universal Turing machine and perform universal computations [20]. The reason comes from a feature that for a given set of inputs, it is not predictable whether the computation will halt or not for a universal Turing machine [21, 22], and this feature is implemented in the rules that belong to the fourth class.

A well-known hypothesis called the *edge of chaos* is suggested to describe the transition phenomenon observed in CA patterns once a small perturbation is introduced to fourth class rules. What we expect from the hypothesis is that the new obtained rule due to the perturbation must either generate a simple pattern or a chaotic one (Table 2.1). In order to quantitatively describe the transition, Packard and later

Langton introduced a parameter (today known as Langton parameter) λ which for each ϕ, $\lambda(\phi)$ is the fraction of the non-zero maps in the transition rule table [23, 24]. Langton showed that such a simple measure is connected to the system behaviour. As λ goes from 0 to 1, different patterns ranging from homogeneous patterns to chaotic ones are produced. At $\lambda = 1/2$ the statistical average over different behaviours shows chaos. Therefore, the rules which $\lambda \sim 1/2$, are at the *edge of chaos*. But later works of Mitchel and Crutchfield showed different results form Langton's. They have shown that even at lower λ chaotic behaviour can be expected, but most of the rules which are at the edge aggregate around $\lambda = 1/2$ [25, 26]. The difference between the results of Langton and Mitchel is due to the different statistical averaging methods, which is extensively discussed in Ref. [25].

Table 2.1 *Rightmost column (rule 110) is perturbed by changing one of its rows, for example changing the first row from 0 to 1 yields the rule 111. Thus there are eight perturbed rules. The last row is the Langton parameter calculated for each rule. The rule 110 belongs to the fourth class. Among the perturbed rules, three of them belong to the class three, three of them belong to the class two, and the rest two belong to the first class. At first glance, this table confirms the hypothesis and shows that the rule 110 is at the edge of chaotic and steady-state periodic regimes, but as it has been mentioned this is not true for all the cases.*

Rule / Initial state	111	108	106	102	126	78	46	228	110
(000)	1	0	0	0	0	0	0	0	0
(001)	1	0	1	1	1	1	1	1	1
(010)	1	1	0	1	1	1	1	1	1
(011)	1	1	1	0	1	1	1	1	1
(100)	0	0	0	0	1	0	0	0	0
(101)	1	1	1	1	1	0	1	1	1
(110)	1	1	1	1	1	1	0	1	1
(111)	0	0	0	0	0	0	0	1	0
λ	3/4	1/2	1/2	1/2	3/4	1/2	1/2	3/4	5/8

So far only one-dimensional CA are discussed. Although the two-dimensional CA are more relevant to this thesis work, one-dimensional CA give an overall picture of the nature of these automata. In contrast with their elementary nature, complex patterns are generated and a variety of rules can be constructed. Next, two-dimensional CA are introduced, which are the underlying structure for charge control studies. The reader is instructed to find more information on one-dimensional CA and deeper analysis of the transitional rules and their classes in Refs. [19, 20, 27].

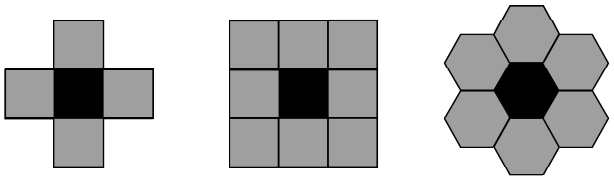

Figure 2.6 *Different lattices with different neighbourhood sets. The hexagonal structure is equivalent to the Moore lattice. Other lattices such as triangular or hexagonal lattices, are an extension to the Moore lattice. The extension to the neighbourhood set increases the complexity of the transitions and the number of possible rules.*

2.1.2 Two-dimensional cellular automata

Historically, the CA first used by von Neumann was a two-dimensional CA capable of self-producing characteristics [3]. Depending on the lattice geometry and the convention of the neighbouring cells on the lattice structure, a variety of CA can be constructed. Among the many variations, there are two generic two-dimensional CA which are known as *von Neumann* and *Moore* CA [19]. They have the same lattice structure, a simple square lattice, but the set $\mathcal{N}_i$ is different for the i_{th} cell.

Going from one-dimensional to two-dimensional CA brings more complexity into the system and makes them more suitable for direct comparison with real-world physical systems. Also different interface structures can be realised by employing different lattice structures at the boundary. This not possible in one-dimensional CA.

Conway's game of life

Conway, a British mathematician, was thinking of a rule which is simultaneously simple in explanation and difficult in prediction. His work [6], was an attempt to generalise the works of von Neumann, Fredkin and Ulam. Conway imposed a set of criteria which the rule must satisfy. The first criterion is that a simple initial pattern does not grow without a limit and, secondly, the pattern produced by the rule does not yield a trivial final state. Besides, the initial pattern must evolve for infinitely many iterations before it falls into either a stable or an oscillatory state.

The underlying structure Conway considered was a two-dimensional simple square lattice with the *Moore* neighbourhood. The rule given by Conway is an elementary two-dimensional rule. Its simplicity and its ability to produce sophisticated patterns attracted many mathematicians and other scientists from different branches

to consider this evolutionary automata for the realisation of real-world systems.

Definiton of life: The rule which Conway defined, associates to the cell with $\sigma = 1$ an attribute *alive* and to those with state $\sigma = 0$ an attribute *dead*. Hence, each cell represents a population which could either grow or decay. The three rules for Conway's CA are as follows:

- *BIRTH*: If a *dead* cell has exactly three *alive* neighbours, it becomes *alive*.
- *DEATH*: A *living* cell with either one *living* cell or no *living* cell in its neighbourhood will die; also a *living* cell will die due to overcrowding if it has more than three *living* neighbours.
- *SURVIVAL*: A *living* cell will continue its *life* if it has 2 or 3 *living* cells in its neighbourhood.

This famous quote by Conway, *"It is probable, given a large enough Life space, initially in a random state, that after a long time, intelligent self-reproducing animals will emerge and populate some parts of the space"*, elucidates the potential of the *'Game of Life'* cellular automaton in describing a specific population growth. This cellular automaton belongs to the fourth class (complex ordered patterns). More interestingly, this cellular automaton is capable of *universal computation*. Its relation to the *Halting theorem* implies that with an initial starting configuration, in general, one cannot predict whether a population will grow or eventually die. In other words it is impossible to predict the outcome of this machine.

3. QUANTUM DOTS

Quantum dots (QDs) are essential systems considered throughout this thesis. Although the technical concerns of their fabrication are not really necessary to understand and follow the text, a brief introduction on how they are constructed, may be beneficial for the reader.

QDs were first fabricated in 1980's and soon after that they found their way to many applications ranging from transistors to LEDs and diode lasers. QDs are semiconductor nanostructures which exhibit discrete energy spectrum, like natural atoms. Due to this property they are called *artificial atoms* [28]. In semiconductor QDs, the motion of the conduction band electrons and valence band holes in space is confined. This confinement is usually created by external electrostatic potentials such as impurities, external electrodes, or by decreasing the spatial dimension to the semiconductor surface [29, 30]. The size of a QD depends on the technique which is used to construct them. Colloidal semiconductor nanocrystals have a size ranging from two to ten nanometres, while self-assembled QDs can have a size between 10 an 50 nanometres. For larger sizes, lateral QDs exceed 100 nanometres [31].

The discrete energy spectrum in QDs has a different nature with respect to the spectrum in real atoms. In atoms, the spectrum is due to the potential of the positively charged nucleus, meanwhile in QDs the electrons are trapped in a potential well. The significant difference therefore becomes evident: in artificial atoms the electron-electron interactions are more important, whereas in real atoms the electron-nucleus interaction (for low atomic numbers) is dominant.

To understand the nature of QDs, their fabrication is elucidated in the following. The next section is dedicated to the implementation of QDs in cellular automata and to their role in computation.

As mentioned previously, there are various methods for the realisation of QDs with different sizes. One of the most frequent method which is used to create QDs in a semiconductor heterostructure is lithography, i.e. depositing metal electrodes on the heterostructure surface. The deposition is carried out by beam epitaxy on het-

erostructure materials which produces a gate pattern. By applying an electrostatic voltage, the potential can be tuned, which leads to the confinement of the electrons and holes on the surface.

Heterojunctions are an important class of junctions that two semiconductor materials with the same lattice constant but different band gaps form. The discontinuity in the energy band after the alignment of the Fermi levels of the two semiconductors, is the key element of the 2DEG formation. In order to find the band gap bending, it is necessary to consider the band discontinuity and solve the Poisson equation across the junction and include the boundary conditions. The n-type AlGaAs has a discontinuity in the conduction band and this allows the electrons to either tunnel or overcome the barrier and gather in the potential well formed in GaAs. This will shift the Fermi level above the conduction band in GaAs and bring it near to the interface. This narrow well in the conduction band of GaAs confines the electrons within a narrow region where 2DEG forms. The high mobility is due to the fact that the electrons come from AlGaAs, where there are very few impurities to scatter the electrons. The scattering process is dominated by the phonon-electron scattering. Therefore, to reduce the scattering, low temperatures are required. GaAs/AlGaAs heterostructure is an example of this class. After doping AlGaAs with Si, the excess electrons will fill the interface within a depth of the order of 10 nanometers. Effectively, in such a thin layer, electrons are confined in the two-dimensional space (z-direction is frozen) and form the two-dimensional electron gas (2DEG) (Fig. 3.1).

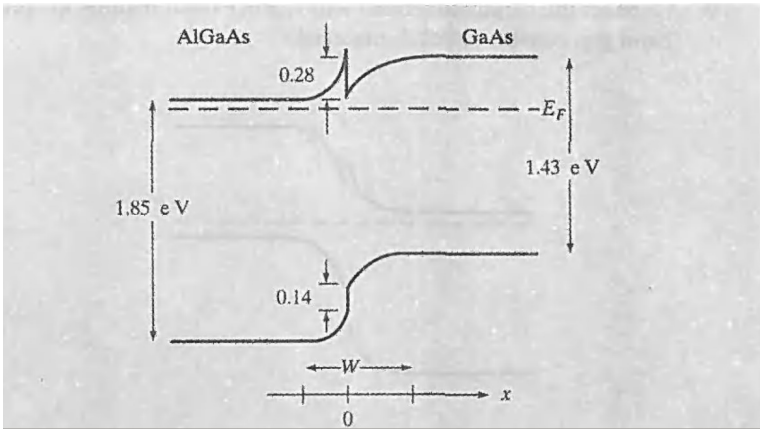

Figure 3.1 *Formation of the 2DEG. Figure adopted from Ref. [30]*

Due to the decrease in geometrical dimensions, and since the donor Si atoms share relatively small number of electrons, which implies low density, the 2DEG possesses a high mobility. By placing charged gate electrodes on top of the heterostructure and applying an electric field by this means, the 2DEG can be locally depleted. The electrode gates are made by epitaxial growth and their thickness is in the range of

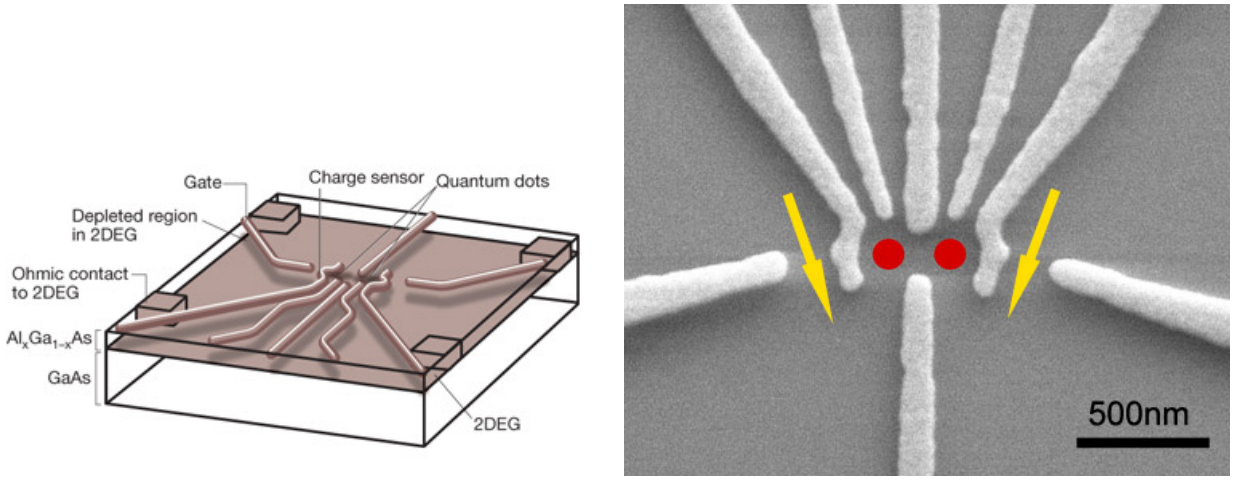

(a) **(b)**

Figure 3.2 *Schematic view of a double quantum dot. The ohmic contact point makes it possible to connect the substrate and the electrodes to the external electrostatic voltage. The 'charge sensors' are quantum point contacts to measure the electron flow the source to drain. The depleted region is shown as the shadow of the electrodes. Figure is adopted from Ref. [32]. (b) Scanning electron microscope micrograph of a double quantum dot. In the figure the surface of the AlGaAs/GaAs heterostructure is shown in dark grey. The light grey regions show the gates (electrode connected to an electrostatic potential) made of gold. The gate locally depletes the 2DEG and forms two tunnel-coupled quantum dots which are shown with red circles. The two yellow arrows are called quantum point contacts which are used to measure the electron flow from the source to the drain. Precise construction of quantum point contact allows us to count the electrons with the precision of one electron. Figure is adopted from Ref. [33].*

the layer depth. This gives the ability to control the depletion locally. A suitable geometrical formation of gates will produce QDs in such a way that a small domain of the space will be partially isolated from the rest.

An important phenomenon in QDs is the *Coulomb blockade effect*. This effect is the key element of the electronic transport through QDs. In Fig. 3.2(a) the ohmic contact weakly connects the QD to the source and drain by tunnel barriers. These barriers are thick, and the transport is dominated by the resonances due to quantum confinement. An extra electron can be added to the QD if its energy overcomes the expectation value of the repulsion energy between the electrons due to the Coulomb repulsion. This electrostatic energy is estimated by $N(N-1)e^2/2C$, where N is the number of the confined electrons and C is the capacitance of the dot. As the number of confined electron increases, the addition of an extra electron to the dot requires more energy. The required energy is therefore Ne^2/C. Division of this energy by the number of the electrons is simply e^2/C which is called the *charging energy* (Fig. 3.3). If this energy exceeds the thermal excitations which are of the order of k_BT, the electrons cannot tunnel through the barriers by the means of

thermal excitations, and therefore the transport is blocked. This effect is known as Coulomb blockade [34–37].

In Fig. 3.3 a schematic representation of this effect is given. In this figure, a QD is connected through its ohmic contacts to the *source* and *drain* and to an external voltage gate. The external voltage gate depletes the 2DEG and forms an electron island. The aforementioned voltages are denoted by V_s, V_d, and V_g, respectively. V_g is set to a constant, and the voltages of the source and drain are varied. They are initially set to values such that the Fermi level of the QD is below the *source* and *drain* energy levels (note that we are in the zero temperature regime, therefore the terminology of the Fermi energy is well-defined.). Due to the geometrical properties of the QD, it has a capacitance, into which the presence of electrons gives a finite contribution. Therefore, as the number of electrons increases in the QD, the Fermi level of the dot will eventually reache the energy level of the *drain*, which leads to escape of the electrons from the dot, and to a contribution to the electric flow.

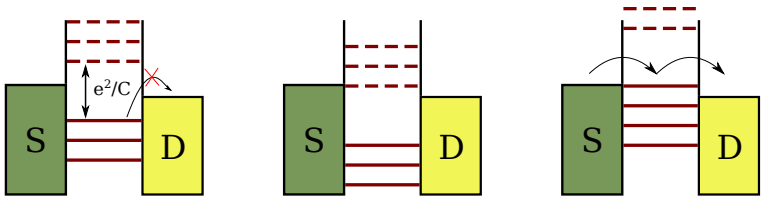

Figure 3.3 *From left to right: The Fermi level of the dot is located below the source and drain energy levels. If the height difference between the energies is higher than the thermal energy, electrons cannot tunnel through the barrier and exit the dot. The letters S and D denote the source and drain, respectively. The energy levels of the dot are illustrated by solid red lines. Each of these levels is occupied by one electron. The dashed lines denote the empty electron states of the dot and are called affinity states. In the middle figure, V_g is increased which leads to the lowering of the energy states of the dots. If the voltage gate is increased further, the energy of the first affinity state becomes equal to the energy level of the source. Therefore, electrons can move from the source to the quantum dot. Since the energy level of these electrons is higher than the energy level of the drain, the electron leaves the dot, which leads to a current from the source to the drain (rightmost figure). After this stage, if V_g is increased further, the highest energy level of the dot, which is aligned with the source, will be lowered and the conductance will be blocked.*

In finite temperatures, the Fermi level corresponds to the chemical energy of the QD, that is, $\mu = \mathcal{E}(N) - \mathcal{E}(N-1)$, where $\mathcal{E}$ is the energy of the QD in its ground state. Based on the explanation above, it is clear that the conductance of a QD must show a rapid jump. When the number of electron tends to infinity, the conductance becomes linear. This can be observed in Fig. 3.3. When the number of electrons increases, the energy gap between the states shrinks and becomes continuous, and the highest energy level will reach the chemical energy of the *drain* (μ_d), and electrons can freely enter the QD from the *source* and escape the dot. In the linear regime,

$\mu_s - \mu_d = -e(V_s - V_d)$ is much larger than the spacing between the energy states. In finite temperatures, electrons may also have a chance to escape form the dot due to thermal excitations; thus the conductance at high V_g does not have regions which correspond to zero conductance (at zero temperatures the profile of the conductance must still show fluctuations between finite and zero conductance. But an interesting effect may be observed in a case where the number of electrons in the dot is infinite. That is the observation of conductance due to the quantum fluctuations in the vacuum.)

So far we have discussed the fabrication and transport mechanism of quantum dots. When quantum dots are in contact with each other their behaviour becomes more complex. In the following sections we consider two QDs in contact, namely double quantum dots. But first, an introductory section about quantum computing and information will be given, since there are some terminologies which are used for the description of double quantum dots. The connection between quantum dots and computation eventually becomes clear in Sec. 2.2.

3.1 Quantum computing and information

Before starting this section, it should be emphasised that this thesis focuses on charge control in quantum dot cellular automata. Although the term *quantum* is used, the computation with these devices is classical. This introduction is given only to familiarise the reader with the concept, since quantum dots are related to both classical and quantum computations.

The very fundamental element of information is a *bit*. The foundation of computation and information is based on the Boolean algebra and Boolean rings. The set of variables of this algebra consists of only two elements, *true* and *false*, which are denoted by 1 and 0, respectively [16, 38]. A bit is therefore either 0 or 1. In classical computation and information the realisation of these two variables may correspond to receive a signal pulse or not. But at any instant it is either on or off. These two states do not coexist even before any measurement. In the quantum counterpart the situation is different. First of all, to distinguish the bits which are used in classical computation and quantum computation, the name *qubit* is considered for the latter case. In quantum computation, qubits coexist prior to the measurement. This is due to the *superposition* principle in quantum mechanics. But after the measurement the situation coincides with the classical regime.

Any physical system with a two-dimensional Hilbert space can be served as a qubit.

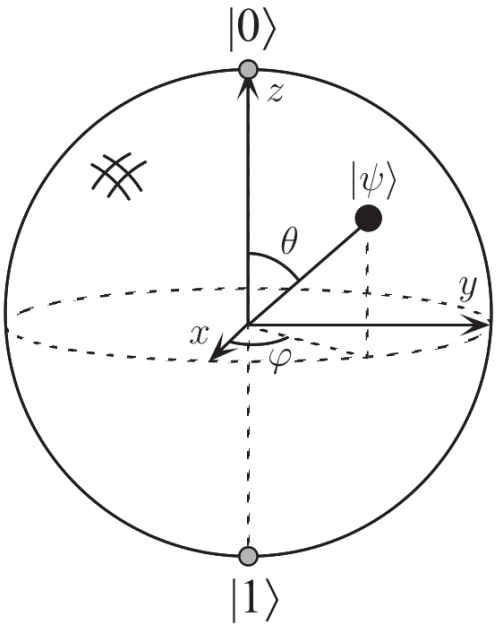

Figure 3.4 *Phase space of a quantum system with a two-dimensional Hilbert space with basis states $|0\rangle$ and $|1\rangle$ represented by the Bloch sphere. The bases are aligned parallel with respect to each other: one points to the positive direction of the z-axis ($|0\rangle$) and the other to the negative direction ($|1\rangle$). The qubit state given by Eq. (3.1) can be rewritten as $|\psi\rangle = \exp^{i\gamma}\left(\cos\frac{\theta}{2}|0\rangle + \exp^{i\phi}\sin\frac{\theta}{2}|1\rangle\right)$, where γ is an arbitrary phase, and θ and ϕ are polar and azimuthal angles, respectively. Figure from Ref. [39]*

Let us call these two basis stets $|0\rangle$ and $|1\rangle$ which are obviously orthonormal. Therefore, any state of the system can be written in the form of a superposition of these two states.

$$|\psi\rangle = \alpha|0\rangle + \beta|1\rangle, \quad |\alpha|^2 + |\beta|^2 = 1. \tag{3.1}$$

For instance, a spin-1/2 system with two orthonormal basis states $|-1/2\rangle$ and $|1/2\rangle$, which correspond to spin-down and spin-up states of an electron, or a photon with orthonormal bases $|L\rangle$ and $|R\rangle$ (left and right circular polarisation), can be served as a qubit. These bases are known as *computational basis states*, and α and β are complex numbers. Therefore, a qubit can possesses a continuum state between $|0\rangle$ and $|1\rangle$. This is counter-intuitive to our common sense with respect to the definite state of classical bits. In order to describe a qubit by classical bits, an infinite sequence of classical bits is required. Once a measurement is carried out on a qubit, its state will collapse into the state $|0\rangle$ with probability $|\alpha|^2$ or into the state $|1\rangle$ with probability $|\beta|^2$. This the only information one can get from a qubit.

A qubit can be represented by a sphere called *Bloch sphere* named after the physicist *Felix Bloch*. It is a geometrical representation for two basis quantum systems and it is especially utilised for the representation of qubits (Fig. 3.4).

Although a qubit can store an infinite amount of classical information, it is important to bear in mind that for quantum computing we need more than one qubit. In order to have a quantum speed-up in the computation, another feature of quantum mechanics is necessary; *quantum entanglement*. An exponential speed-up of quan-

tum computers with respect to classical computers requires dynamics which cannot be efficiently simulated on classical computers [40]. Very well-known states for understanding the role of entanglement are the Bell states. They are also commonly called *EPR pairs*. They are the most simple two-qubit states which are maximally entangled. The Bell states, which can be constructed from two successive two-qubit gate operations [39], are listed below:

$$
\begin{aligned}
|\beta_{00}\rangle &= \frac{1}{\sqrt{2}}\left(|00\rangle + |11\rangle\right), \quad |\beta_{01}\rangle = \frac{1}{\sqrt{2}}\left(|01\rangle + |10\rangle\right), \\
|\beta_{10}\rangle &= \frac{1}{\sqrt{2}}\left(|00\rangle - |11\rangle\right), \quad |\beta_{11}\rangle = \frac{1}{\sqrt{2}}\left(|01\rangle - |10\rangle\right).
\end{aligned} \tag{3.2}
$$

It can be observed that, once a measurement is done on the first qubit, the state of the second qubit will be known instantaneously. This property is important for quantum algorithms such as Shor's prime factorisation [41], superdense coding [42], and also especially in the field of quantum cryptography such as BB84 encoding scheme for public key distribution [43].

Entanglement is also important when one thinks of quantum simulations on classical hardware. Generally, a many-body quantum system consisting of n particles requires $\mathcal{O}(\exp(n))$ parameters to be fully described. Therefore, not all quantum dynamics simulations can be carried out on classical computers. This consideration puts a limit on the amount of entanglement. Vidal [40], has shown that quantum computing with pure states of n interacting particles can be efficiently simulated on classical computers, if the entanglement present in the simulation does not exceed a certain level.

In order to manipulate bits or qubits we need logical operations. They are called *logic gates*. Suppose an operation which transforms $|0\rangle \rightarrow |1\rangle$ and $|1\rangle \rightarrow |0\rangle$. Thus, the action of such a logic gate on the qubit $|\psi_{in}\rangle = \alpha|0\rangle + \beta|1\rangle$ yields $|\psi_{out}\rangle = \alpha|1\rangle + \beta|0\rangle$. This is an example of single-qubit class of logic gates and corresponds to the classical **NOT** gate. The **NOT** gate simply interchanges the bits. Its matrix representation can be written as follows:

$$
X \equiv \begin{pmatrix} 0 & 1 \\ 1 & 0 \end{pmatrix}. \tag{3.3}
$$

Input	Output
$\|00\rangle$	$\|00\rangle$
$\|01\rangle$	$\|01\rangle$
$\|10\rangle$	$\|11\rangle$
$\|11\rangle$	$\|10\rangle$

Table 3.1 *Truth table of the* ***CNOT*** *gate; a two-qubit gate which stands on controlled NOT. The state of the second qubit remains unchanged if the value of the first qubit is true ($|0\rangle$), otherwise its state would be flipped upon the action of the gate.*

In contrast to classical computation with **NOT** as the only non-trivial single-bit logic gate, in quantum computation any operation that preserves the norm of the qubit is a valid logic gate. In other words, the matrix that represents the gate must satisfy the *unitarity* condition. Another interesting gate is called the *Hadamard* gate. Its matrix representation is given by

$$H \equiv \begin{pmatrix} 1 & 1 \\ 1 & -1 \end{pmatrix}. \tag{3.4}$$

Application of the Hadamard gate accompanied by the **CNOT** gate, which is a two-qubit gate, on $|00\rangle$, $|01\rangle$, $|10\rangle$, and $|11\rangle$ yields the Bell states listed in Eq. (3.2).

Another issue worth of attention is the linearity of the action of the gates. This is due to the fact that the Copenhagen interpretation of quantum mechanics is a linear formalism (algebra of linear operators [44]). There are other interpretations with the formalism beneath that are non-linear. It has been shown for instance by Gisin and Polchinski that non-linearity would violate the causal property of physical events (superluminal transport). Based on this result, they have predicted superluminal communications in experiments concerning the EPR paradox [45–47] (EPR paradox, after Einstein, Podolsky and Rosen, was introduced to address the incompleteness of the physical reality described by quantum mechanics. For further reading we refer to [48–54]).

This introductory section on quantum computing and information was given to familiarise the reader with the concept, and to clarify any possible ambiguity that may arise in the rest of the text. In this thesis, only one-electron systems have been considered. Therefore, one should not expect to perform quantum computation with these devices. Even in the case of many-body systems, which is not considered in this thesis, a certain level of entanglement must exist for quantum computation and information processing.

3.2 Double quantum dots

Double quantum dots (DQDs) are systems that consist of two quantum dots which are either weakly or strongly coupled to each other. These two classes are commonly referred to ionic and covalent bondings [55]. In the former case, the electrons are localised in only one QD. The excess or lack of the expectation number of electrons in either dot causes an effective Coulomb attraction which itself leads to a stable structure [35]. In the latter case, instead the wave function of the electrons is spread over both QDs. Therefore the electrons can tunnel spontaneously between two dots before a measurement on their spatial coordinates.

The two QDs can be coupled to each other in three different ways. They can be coupled in series [56–60], parallel [61–63], or they can be coupled to each other vertically [64–66]. Meanwhile in the first two cases the characteristics of the tunnel-barrier depend on the voltage gate and the geometry, in the latter case the tunnel-barrier properties are identified by the growth parameters of the material in use.

The difference between the serial and parallel DQDs is that in the former case the dots, source, and drain are attached to each other in series (Fig. 3.5), while in the latter case each dot is attached to the source and drain separately. Besides, the profiles of the Coulomb blockade resonant peaks is totally different for the two cases. In series coupled DQDs, the Coulomb blockade peaks initially the peaks correspond to the two separate quantum dots is observed and eventually the peaks of a one large unified quantum dot appear [67]. In parallel setting, there are also secondary peaks in the Coulomb blockade spectrum profile due to quantum mechanical inter-dot tunnelling [63].

A strongly coupled DQD is quite similar to a case when two real atoms form a covalent bond. Once the QDs are brought together, a hybrid energy state is formed due to the overlap of their ground states, which causes the lowering the total ground state energy of the whole system. It worth mentioning that in the ionic case, where Coulomb interaction (classical interaction) forms the binding between the two dots, in the covalent case the binding is due to the quantum mechanical properties of the electrons and the consequence of the Pauli's exclusion principle, that is the key element of the formation of the bond. It is possible to observe a transition between weakly coupled and strongly coupled QDs by modifying the tunnelling barrier. The strength of the bond between the dots can be determined quantitatively by microwaves. Irradiation of microwaves causes photon assisted tunnelling (PAT) in coupled QDs. The mechanism is based on the *inelastic* tunnelling of the electron between the two dots and exchange of energy with an applied external time-varying

potential. Further theoretical explanations can be found in [68, 69].

Regardless of the number of QDs in a system, a stability diagram, is a common tool to study the transport properties of the system [70]. The dimension of the diagram is simply the number of QDs which are coupled to each other. This makes it clear that for a system which has four QDs or more, the method loses its advantages in representing the stability diagram, since the visualisation of such a diagram becomes complicated.

3.2.1 Stability diagram

The purpose of the stability diagram is to understand the equilibrium charge state of the system. There are two regimes of transport phenomena: classical regime and quantum mechanical regime. In the classical regime the effect of discrete quantum states is not of concern [70]. In the latter case, shifts in the energy levels due to addition or loss of electrons must be considered (explanation will be given later).

As depicted in Fig. 3.2(b), a DQD can be modelled as a circuit with tunnel resistors and capacitors (a schematic view is given in Fig. 3.5)

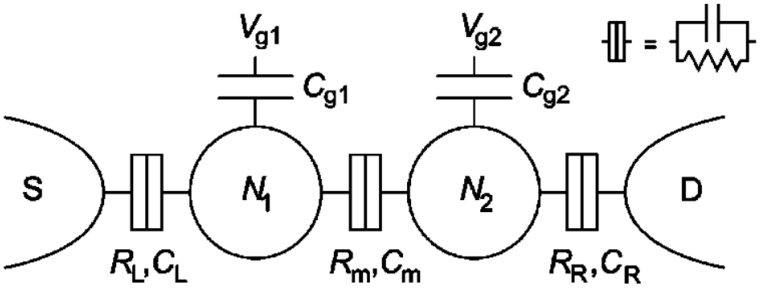

Figure 3.5 *Double quantum dot in series modelled by tunnel resistors and capacitors. The symbols are explained in the text. The schematic is simplified according to the inset. The figure is adopted from Ref. [55].*

In the figure above, each dot is represented by a circle with its corresponding number of electrons N_i which is connected through the capacitor C_{g_i} to the voltage gate V_{g_i}, where i is the index of the dot and the index g refers to the *gate*. The first dot is connected to the *source (S)* through the tunnel resistor R_L, and the capacitor C_L and the second dot is connected to the *drain (D)* through the tunnel resistor R_R and the capacitor C_R. The coupling between the two dots is modelled by the tunnel barrier represented by R_m and C_m. In the linear regime (the bias voltage V between the *source* and *drain* is almost zero), the electrostatic energy of the system is given by

$$U(N_1, N_2) = \frac{1}{2}N_1^2 E_{C_1} + \frac{1}{2}N_2^2 E_{C_2} + N_1 N_2 E_{C_m} + f(V_{g_1}, V_{g_2}) \tag{3.5}$$
$$f(V_{g_1}, V_{g_2}) = \frac{1}{e}\left[C_{g_1}V_{g_1}(N_1 E_{C_1} + N_2 E_{C_m}) + C_{g_2}V_{g_2}(N_1 E_{C_m} + N_2 * E_{C_2})\right] + \frac{1}{e^2}\left[\frac{1}{2}C_{g_1}^2 V_{g_1}^2 E_{C_1} + \frac{1}{2}C_{g_2}^2 V_{g_2}^2 E_{C_2} + C_{g_1}V_{g_1}C_{g_2}V_{g_2}E_{C_m}\right].$$

E_{C_i} is the *charging energy* of the i_{th} dot. Since the two dots are coupled with each other, the energy change in either dot due to the addition of one electron will affect the energy of the other one; E_{C_m} accounts for this energy change and is called *electrostatic coupling energy*. These three energies can be be expressed solely in terms of the capacitance of each dot and the coupling capacitance as follows:

$$E_{C1} = \frac{e^2}{C_1}\left(\frac{1}{1-\frac{C_m^2}{C_1C_2}}\right), \quad E_{C2} = \frac{e^2}{C_2}\left(\frac{1}{1-\frac{C_m^2}{C_1C_2}}\right), \quad E_{C_m} = \frac{e^2}{C_m}\left(\frac{1}{\frac{C_1C_2}{C_m^2}-1}\right). \tag{3.6}$$

The notation C_i refers to the sum of all capacitances attached to the i_{th} dot ($C_{1(2)} = C_{L(R)} + C_{g_{1(2)}} + C_m$). For the sake of consistency in the explanation of the equation above, the two limiting cases will be examined. First, consider the limiting case in which the two dots are uncoupled, which implies that the coupling capacitance C_m tends to zero. In this case, $E_{Ci} = \frac{e^2}{C_i}$ is the *charging energy* of a single uncoupled quantum dot and $E_{Cm} \to 0$. Thus, the equation (3.5) reduces to

$$U(N_1, N_2) = \frac{(N_1 e + C_{g_1}V_{g_1})^2}{2C_1} + \frac{(N_2 e + C_{g_2}V_{g_2})^2}{2C_2}, \tag{3.7}$$

which is simply the sum of the electrostatic energies of two uncoupled quantum dots. The other limiting case is such that the two dots are tightly coupled to each other and the coupling capacitance becomes dominant ($C_m \gg (C_{g_i}, C_{L(R)})$). Therefore the electrostatic energy of the system becomes

$$U(N_1, N_2) = \frac{[(N_1 + N_2)e + C_{g_1}V_{g_1} + C_{g_2}V_{g_2}]^2}{2(C_1' + C_2')}, \tag{3.8}$$

where $C_i' = C_i - C_m$. From the term $(N_1 + N_2)e$ it can be deduced that the two quantum dots are merged and form a single quantum dot with capacitance $C_1' + C_2'$. It can be also seen that in this case $E_m \to \infty$. This implies that the addition of one electron to one quantum dot will change the energy of the other dot by an infinite amount. This could be interpreted as the self-energy of the additional electron, since the two dots are merged and form a single dot.

Since the number of electrons in QDs changes, the possible states of the system in thermodynamic equilibrium are represented by the *grand canonical ensemble* [71]. Since the system (two QDs) is in the thermodynamic equilibrium (chemical equilibrium) with the reservoir (*source* or *drain*), the electrochemical potential μ is a relevant quantity for the description of the system. The electrochemical potential of the i_{th} dot is the energy required to add an extra electron to it while keeping the number of the electrons of the other dot constant:

$$\begin{aligned}\mu_1(N_1, N_2) \equiv & U(N_1, N_2) - U(N_1 - 1, N_2) \\ = & \left(N_1 - \frac{1}{2}\right) E_{C1} + N_2 E_{Cm} - \frac{1}{e}(C_{g1} V_{g1} E_{C1} + C_{g2} V_{g2} E_{Cm}); \qquad (3.9) \\ \mu_2(N_1, N_2) \equiv & U(N_1, N_2) - U(N_1, N_2 - 1) \\ = & \left(N_2 - \frac{1}{2}\right) E_{C2} + N_1 E_{Cm} - \frac{1}{e}(C_{g1} V_{g1} E_{Cm} + C_{g2} V_{g2} E_{C2}). \qquad (3.10)\end{aligned}$$

By a simple arithmetic calculation (at constant gate voltage), $\mu_1(N_1 + 1, N_2) - \mu_1(N_1, N_2) = E_{C1}$. This energy is called the *addition energy* of dot 1 and is simply the *charging energy*. In a similar way, $\mu_2(N_1, N_2 + 1) - \mu_1(N_1, N_2) = E_{C2}$. It has to be emphasised that this conclusion is true only in the classical treatment of the system. In the quantised regime, once an extra electron enters the dot, discrete energy levels of the dot also play a role in the electrochemical potential and the *addition energy* is not equal to the *charging energy* and they differ by an amount ΔE, which is the difference between the energy state which will be occupied by the extra electron and the highest energy level occupied before its addition (one has to care about the change in the energy state levels after the addition of the extra electron to the dot).

Now the charge stability diagram can be plotted by the means of Eqs. (3.9) and (3.10) (Fig. 3.6). The diagram shows the change in the numbers of the electrons in the dots if the gate voltages V_{g1} and V_{g2} are varied. Since we have considered zero bias voltage, if either $\mu_1(N_1, N_2)$ or $\mu_2(N_1, N_2)$ exceeds zero electrochemical

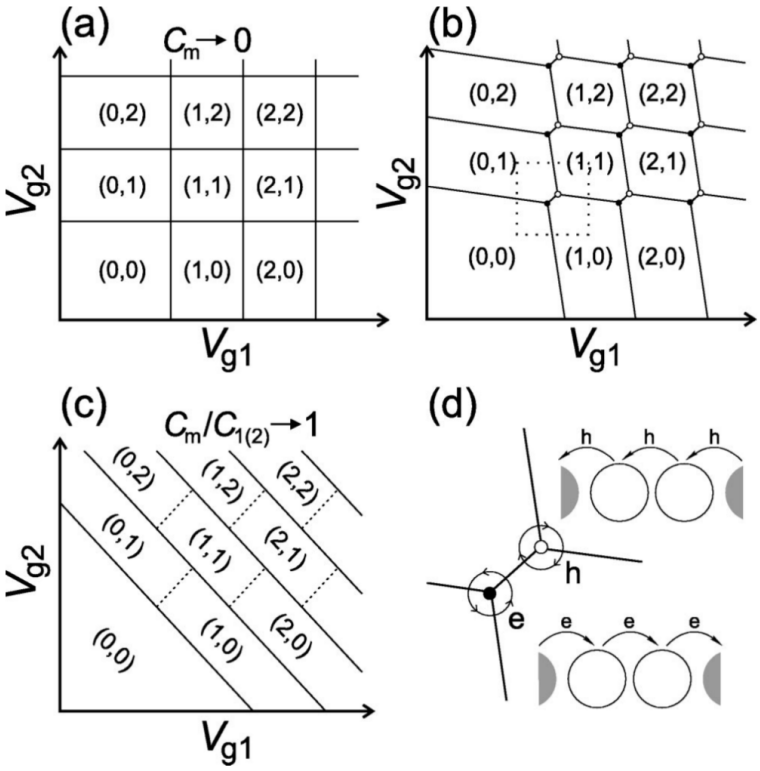

Figure 3.6 *(a) Two uncoupled quantum dots. The charge of the quantum dots is changed independently of each other. (b) Two coupled quantum dots. The two triple points are inside the dotted square. The transport due to the electron displacement is shown by filled black circles. In this case the charge state of the system changes from* $(0,0) \to (1,0) \to (0,1) \to (0,0)$ *(corresponds to the anticlockwise cycle shown in (d)). The conductance due to the hole transport is shown by empty white circles which corresponds to a cyclic process* $(1,1) \to (0,1) \to (1,0) \to (1,1)$*. This is the clockwise cycle shown in (d). In this type of conductance, a hole enters the first dot and cancels the negative charge of the electron. Then it moves to the second dot and after that leaves the dot. (c) The limiting case of tightly coupled quantum dots. Since the two dots become a single dot, the line segment connecting the two triple points becomes infinite. Therefore the states for which* $N_1 + N_2$ *is the same become indistinguishable.*

potential (the electrochemical potential of the leads is zero), an electron would escape the dot. Therefore the number of electrons in the dots which determines the charge equilibrium state would be the largest integers N_1 and N_2 such that both electrochemical potentials are negative. The equilibrium constraint and the fact that N_i's are integers form a hexagonal phase space. In Fig. 3.6(a) the two dots are decoupled ($C_m \to 0$). Therefore the change in V_{g1} only changes N_1 and leaves the charge state of the second dot unaffected. In this case the charge stability diagram is not a hexagonal phase space but rather a square. But if the dots are coupled to each other (finite C_m), the vertices of the squares are stretched and two distinct points will be formed. Since these two points belong to three different regions (3.6(b)), they are called *triple points*. At these points, the charge state of the system

is not at equilibrium but rather in a steady state of charge flow between the three distinct regions which share the *triple points*. At these points a measurable current is formed due to the transfer of charge between the three degenerate charge states of the system.

The two triple points refer to different types of charge transport. In Fig. 3.6(d), the two different processes are represented by filled black circles and the other ones by empty white circles. The filled black circles refer to processes where the electrons are the carrier of the current in contrast to the empty white circles in which the charge transport could be considered by the transport of the holes. The conductance in the former case is a cyclic process described as follows:

$$(N_1, N_2) \rightarrow (N_1 + 1, N_2) \rightarrow (N_1, N_2 + 1) \rightarrow (N_1, N_2). \tag{3.11}$$

In the latter case the conductance is due to the following process:

$$(N_1 + 1, N_2 + 1) \rightarrow (N_1, N_2 + 1) \rightarrow (N_1 + 1, N_2) \rightarrow (N_1 + 1, N_2 + 1). \tag{3.12}$$

3.2.2 Double quantum dots and computation

It has been mentioned that polarisations of photons and spin degree of freedom of electrons can be served as qubits, but they are not the only candidates. DQDs can also be utilised for this purpose. Both spin and charge degrees of freedom have a qubit realisation in DQs.

In a singly charged DQD, the presence of the electron in the left dot corresponds to qubit $|0\rangle$ and if it is in the right dot, it corresponds to qubit $|1\rangle$ (the presence of the electron corresponds to the occupation of the ground state energy level) [72]. Recall that the superposition principle is the key element of quantum computation. In a weakly coupled DQD where the electron is localised in one dot, a transition to classical computation occures. But also strong coupling of the QDs requires an increase in the bias voltage, which is the source of decoherency and it is due to the electron-phonon interaction. Besides this cause, there is another source of decoherency which relates to the background electron scattering due to the presence of impurities. The decoherecy times in charge based DQD qubit systems is of the order of nanoseconds (for instance see Refs. [73, 74]. This time scale extends to

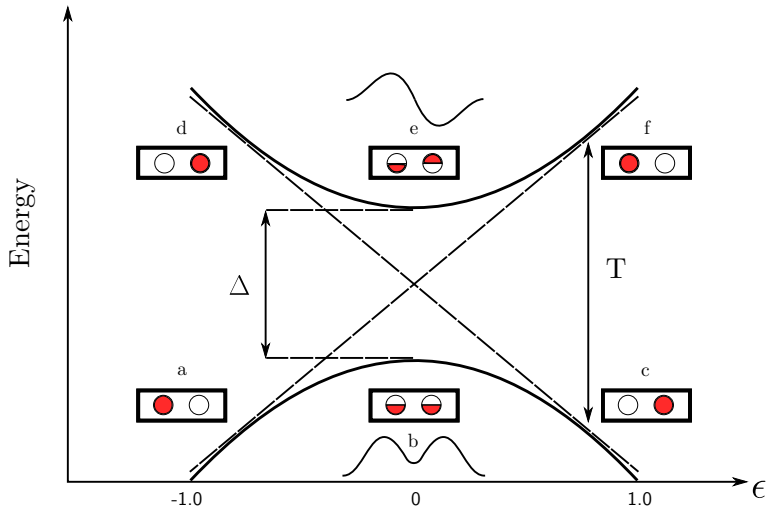

Figure 3.7 *Interplay between bonding and antibonding energy states. At $\epsilon = 0$ the states $|L\rangle$ and $|R\rangle$ are degenerate, so that the state of the DQD is in a superposition of the two eigenstates. The anticrossing energy Δ is the barrier coupling strength which can be controlled by the bias voltage. The points (b) and (e) correspond to the states $\frac{1}{\sqrt{2}}(|L\rangle + |R\rangle)$ and $\frac{1}{\sqrt{2}}(|L\rangle - |R\rangle)$, respectively. T is a measure of the relaxation time between the transition from the antibonding state to the bonding state.*

microseconds for spin-based qubit realisation of DQDs [75, 76]). Therefore, the strength of the coupling must be such that the wave function of the electron spreads through both dots, thus optimising the coherence of the system.

Suppressing the higher energy levels of each QD effectively decreases the dimension of the Hilbert space to two dimensions, and it can be approximated by a two-level system. These two states correspond to bonding and antibonding states (Fig. 3.7).

The Hamiltonian of a two-level system can be written as follows:

$$\mathcal{H} = \epsilon_L|L\rangle\langle L| + \epsilon_R|R\rangle\langle R| + \Delta(|L\rangle\langle R| + |R\rangle\langle L|), \tag{3.13}$$

where ϵ_L and ϵ_R are the ground state energies of the left and right QDs, respectively. Δ is the energy difference between the bonding and antibonding states. The Hamiltonian above has a matrix representation based on Pauli matrices and can be transformed according to the equation below [77]:

$$\mathcal{H} = \frac{1}{2}\epsilon\sigma_z + \frac{1}{2}\Delta\sigma_x. \tag{3.14}$$

Here ϵ is the energy difference between the ground state energies. This expression

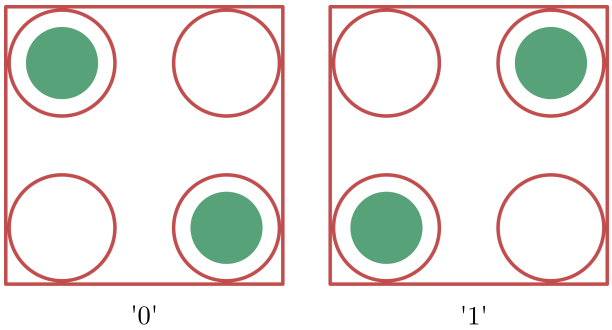

Figure 3.8 *Schematic representation of the primary computational cell in its '0' state (left) and '1' state (right). The quantum dots are shown by red circles and the electron density is shown by filled green circles. The rotational symmetry group of $\frac{\pi}{2}$ plays an important role for diagonal and anti-diagonal distribution of the electron density, which will be explained in the last chapter. If these two cells are in contact with each other, the Coulomb interaction makes the state of the whole system unfavourable. Therefore, the ground state of the whole system will be either '00' or '11'.*

coincides with the description of a spin-1/2 system in a presence of an external magnetic field with components Δ and ϵ along the x-axis and z-axis, respectively. Thus, these two-level DQDs with charge degree of freedom are called *pseudospin qubit* systems. The corresponding energies for the eigenstates of the system are $\mp 1/2\hbar\Omega$, where $\Omega = \sqrt{\Delta^2 + \epsilon^2}/\hbar$. For this system both single and two-qubit gate operations have already been demonstrated [72, 78].

3.3 Quantum dot cellular automata

The aim of the previous sections was to introduce the reader with the concepts of the CA and QDs. Although the fields are rich and more complicated to be fully implemented in this work, the provided information was only given as a necessary introductory for the rest of the material. This section is dedicated to present the quantum dot CA (QCA) structure and its role in logical computation.

The experimental aspect of manufacturing such a system is itself an interesting topic which is quite challenging and still far away from industrial production. Since the topic of this thesis is the controllability of the system, we consciously avoid entering this issue any further. Strictly speaking, QCA are physical realisations of classical CA with an emphasis that they are used typically for *classical computation*. However, there are studies on QCA tailored for *quantum computation* [79].

Designing CA based on QDs is originally a consequence of technological saturation in the power and size of computational devices. The electronics technology of the present devices is based on field-effect transistors (FETs) [80]. They have been

improved over the past three decades exponentially as Moore has predicted in his famous law [2]. Despite the fact that the size has decreased significantly, the density of the transistors in electronic circuits doubles every two years so that there is an exponential growth in the performance of these devices. It is not surprising that this improvement has already begun to saturate, since the decrease in size exhibits quantum mechanical behaviours. For this reason, changing the FET-paradigm necessarily needs departure from microstructure size scale to the nanostructure regime.

Among the different paradigms, QCA are prominent candidates for very two specific reasons. QDs are essentially tunable traps for a defined number of electrons. This gives the ability to control the size of the device, which is of absolute importance. Moreover, utilising QDs in QCA drastically improves the energy consumption. As Landauer's principle [81] indicates, energy dissipation from a logically irreversible binary operation is $k_B T \log(2)$. In a response by Boechler *et al.*, it has been argued that energy dissipation lower than this limit can be achieved for charge-based computation [82, 83].

QCA are QDs positioned on a square lattice structure. The mathematical representation attributes the QDs to the elements of the set $\mathcal{L}$, while the quantum mechanical states of a QD are elements of the set Σ (the sets $\mathcal{L}$ and Σ are defined in Ch. 2 Sec. 1). The primary computational cell consists of four quantum dots attached to square lattice points. The global state of this cell is defined by the charge distribution (this cell has a experimental realisation [84]). To distinguish two possible states to represent bits 0 and 1, conventionally the diagonal and anti-diagonal configurations of the charge distribution correspond to bits 0 and 1, respectively (Fig. 3.8). A collection of these primary cells positioned in an array forms a system in which the state of each cell depends on the states of the other cells. Hence, the specific architectural arrangement of the cells is an important issue one has to bear in mind for the design for logical computation.

The fundamental QCA logic device consists of three input cells called majority logic gates [Fig. 3.9(c)]. Besides, there is a central cell whose state depends on the value of the input cells. The state of the output cell [the rightmost cell in Fig. 3.9(c)] is determined by the state of the central cell. This logical device can act as an OR or an AND gate by fixing the state of one of the input cells A, B or C. The majority gates provide an advantage that any logical function has a realisation circuit based on them [85].

The charge control of the OR gate is demonstrated in Fig. 3.9 and the description is given in the caption.

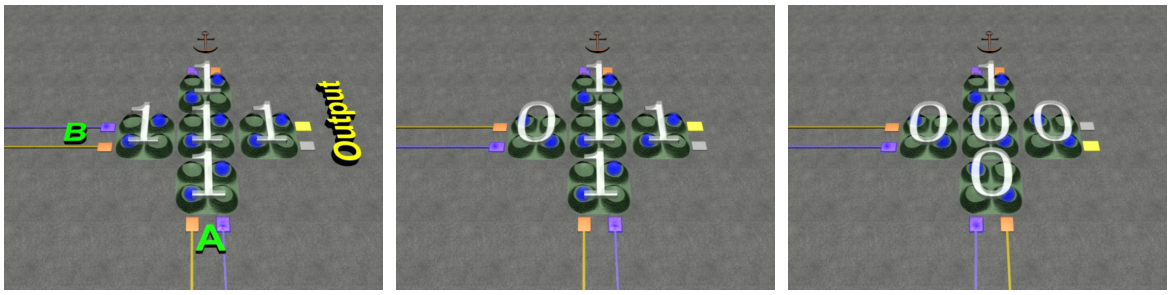

(a) **(b)** **(c)**

Figure 3.9 *OR majority gate. The quantum dots are shown as empty hollow bulbs and the electron density is shown with blue colour. (a) The initial state of the OR gate in which all the primary cells are initiated to state '1'. There are three input primary cells. One of them is frozen and an anchor is shown above it (upper cell). Two remaining input cells are denoted by A and B. (b) The state of the input cell B changes to '0', but the output cell does not change. These is due to the fact that the central cell in its current state minimises the total Coulomb interaction of the whole system. But in (c), changing the state of A to '0', increases the Coulomb interaction and therefore the central cell changes its state to '0' and the output cell changes its state to '0'. A similar architecture can be used for an AND gate with the difference that the upper cell must be fixed in state '0'. The figures are snapshots from a short animation by J. C. Bean [86].*

4. QUANTUM OPTIMAL CONTROL THEORY

Variational calculus is the basis of many control theories such as optimal control theory. Variational calculus can be used even to prove that the shortest distance between two points in an Euclidean space is a straight line [87]. Even Egyptians used this method to find the shortest distance, simply by stretching a rope between two points [88]. The theory is based on the *variational principle*. It has roots in philosophical ideas by many prominent philosophers and scientists of 17th century. Leibniz considered the God as a perfect mathematician that as a supreme being, has created this world in such a way that the occurrence of an event must be as simple as possible and must minimise its action. Maupertuis, with a close opinion to thoughts of Leibniz, announced the famous principle of least action [89]. This work is considered as an extension to the work of Hero of Alexandria on geometrical optics, which is formulated by Pierre de Fermat and is known as *the principle of least time* [90].

Optimal control theory is a mixture of control theory and variational calculus. In general in an optimal control problem, the dynamics of a system of concern is constrained in such a way that certain criteria must be minimised or maximised. Solving the differential equation of motion of the system under the constraints leads to a set of control equations satisfying the imposed criteria. Most probably, the oldest problem which has been solved by this theory is *Brachistochrone* [91].

Optimal control theory has been expanded to quantum mechanics after the realisation of the first laser by Maiman in 1960 [92]. This brought up the idea of coherent control of quantum mechanical systems in a tailored manner by means of electromagnetic fields. For instance, lasers can be implemented for bond breaking in chemical compounds or to control charge flow by selectively exciting certain molecules [93]. But designing an electromagnetic field to achieve optimised control over a system was an absolute obstacle. This became evident when chemists tried to shine a monochromatic light tuned on the resonance frequency of a chemical compound to break a specific bond in the molecule. This naive idea only heated the molecule. It became clear that the solution for this process is not trivial. Since microscopic systems do possess many quantum characteristics such as entanglement, their coherent

characteristics should not be distorted [94].

There are many theoretical methods to find the optimised pulse such as pump-dump control [95], Brumer-Shapiro control [96] and stimulated-Raman-adiabatic-passage (STIRAP) [97]. One principle that these methods share is their intention to control the evolution of the quantum system by controlling a single parameter. As the degrees of freedom increase, single-parameter schemes fail in finding the optimal pulse, and multi-parameter control methods become more vital.

Quantum optimal control theory (QOCT), first introduced and developed in 1980s [98, 99], is a powerful variational method capable to deal with problems underlined above. In QOCT, at the first sight, the outcome could barely give a straightforward understanding about the nature of the system, since QOCT utilises consecutive quantum interferences by optimising both phase and amplitude of the pulse at the same time under physical constraints. Therefore a great amount of outcome information is required to be deeply analysed.

As it has been mentioned, traditionally *laser* fields in the dipole approximation are used for controlling quantum systems and, as a consequence, the formulation of QOCT needs to be justified for local gate pulses. In the following sections, the general concepts of the scheme are introduced and modified equations for the optimisation of local gates will be derived.

4.1 Theory of quantum optimal control

4.1.1 System description

Consider a quantum system with the total Hamiltonian

$$\mathcal{H} = \mathcal{H}_0 + \mathcal{H}_{ext}. \tag{4.1}$$

The wave function $\Psi(\mathbf{r}, t)$ obeys the time-dependent Schödinger equation (in atomic units)

$$i\partial_t \Psi(\mathbf{r}, t) = \mathcal{H}\Psi(\mathbf{r}, t). \tag{4.2}$$

In Eq. (4.1), $\mathcal{H}_0$ consists of the kinetic energy operator $\hat{\mathcal{T}} = \nabla^2/2$ plus the stationary potential $\hat{\mathcal{V}}_0(\mathbf{r})$ that defines the system geometry. $\mathcal{H}_{ext}(t)$ is an external potential introduced to control the system. Generally, the external Hamiltonian can be any kind of energy source, specifically laser field. In this work an external voltage gate is used for controlling the system [100]. Therefore, the external Hamiltonian $\mathcal{H}_{ext}$ is substituted with a local voltage gate $U(\mathbf{r}, t)$, that is, $\mathcal{H}_{ext} = U(\mathbf{r}, t)$. Since the spatial and temporal parts of the voltage gate are independent, the separability condition implies that

$$U(\mathbf{r}, t) = g(\mathbf{r})f(t), \tag{4.3}$$

where $g(\mathbf{r})$ is the static spatial component and $f(t)$ is the component which solely depends on time. This time-dependent part $f(t)$ will be optimised within QOCT.

4.1.2 Lagrange functional

It has been previously mentioned that QOCT is a variational scheme subjected to system constraints. The aim is to find a control pulse $f(t)$ in such a way that starting from a pre-defined initial state of the system, after the interaction time with the field, the system is found in a well-defined desired final state. This means that expectation value of a general operator $\hat{O}$ has to be found in its extremum under the applied field $f(t)$. Mathematically written:

$$\max_{f(t)} J_1 \quad \text{with} \quad J_1[\Psi] = \left\langle \Psi(T) \right| \hat{O} \left| \Psi(T) \right\rangle . \tag{4.4}$$

The functional J_1 is known as the *yield*.

Another intuitive constraint, especially when considering laser pulses of limited power, is the minimisation of the *fluence*, i.e. the time-integrated intensity of the pulse:

$$J_2[f] = -\int_0^T \alpha f^2(t) dt. \tag{4.5}$$

Here T is the field duration and the positive constant α is the penalty factor. α can also be considered as a time-dependent function to dictate the pulse shape at any

given instance of time. This issue has been addressed in Ref. [101].

As another constraint, the wave function has to satisfy the time-dependent Schrödinger equation. The functional expression for this constraint is given by

$$J_3[f, \Psi, \chi] = -2\,\mathrm{Im} \int_0^T \langle \chi(t)| \left(i\partial_t - \mathcal{H}(t)\,|\Psi(t)\rangle\right) dt, \tag{4.6}$$

where $\chi(t)$ is a time-dependent Lagrange multiplier. The choice of the imaginary part of the functional is a matter of convention and consistency with previous works. In this functional the field f is implicitly contained in the Hamiltonian $\mathcal{H}$.

Finally, by summing the expressions (4.4), (4.5) and (4.6) we obtain the Lagrange functional of the system:

$$J[f, \Psi, \chi] = J_1[\Psi] + J_2[f] + J_3[f, \Psi, \chi]. \tag{4.7}$$

This functional represents the standard optimal control problem. By direct variation of this functional, we find the so-called *control equations*.

4.1.3 Control equations

To find the optimal pulse, the total variation of the Lagrange functional with respect to the independent variables Ψ, f and χ must be equal to zero. The solutions are the extremums of the functional. We must note that the solutions of the problem must have a meaningful physical interpretation [102].

$$\begin{aligned}\delta J &= \int_0^T d\tau \int_V d\mathbf{r} \left\{ \frac{\delta J}{\delta \Psi(\mathbf{r},\tau)} \delta\Psi(\mathbf{r},\tau) + \frac{\delta J}{\delta \chi(\mathbf{r},\tau)} \delta\chi(\mathbf{r},\tau) \right\} + \int_0^T d\tau \frac{\delta J}{\delta f(\tau)} \delta f(\tau) \\ &= \delta_\Psi J + \delta_\chi J + \delta_f J. \end{aligned} \tag{4.8}$$

Variations with respect to the complex conjugates of Ψ and χ have been discarded, since they yield the complex conjugate set of equations.

The total variation must be equal to zero in order to find the maximum of functional J. Since the variations with respect to the variables are linearly independent, each individual term must be equal to zero:

$$\delta J = 0 \Rightarrow$$
$$\delta_\Psi J = 0 \quad , \quad \delta_\chi J = 0 \quad , \quad \delta_f J = 0 \tag{4.9}$$

Variation with respect to the wave function

The variation of functionals J_1 and J_2 with respect to Ψ can be taken in a straightforward fashion. But the variation of J_3 needs more effort. For this reason we modify the expression by using integration by parts:

$$\begin{aligned}\int_0^T \langle\chi(t)|\ [i\partial_t - \mathcal{H}(t)]\ |\Psi(t)\rangle\, dt = \\ i\,\langle\chi(t)|\Psi(t)\rangle\,\Big|_0^T - i\int_0^T \langle\partial_t\chi(t)|\Psi\rangle\, dt - \int_0^T \langle\mathcal{H}\chi(t)|\Psi(t)\rangle\, dt = \\ i\,\langle\chi(t)|\Psi(t)\rangle\,\Big|_0^T + \int_0^T \langle(i\partial_t - \mathcal{H})\,\chi(t)|\Psi\rangle\, dt.\end{aligned} \tag{4.10}$$

After this modification, the variation of J with respect to Ψ is readily found to be

$$\begin{aligned}\delta_\Psi J = \left\langle \Psi(T)|\,\hat{O}\,|\delta\Psi(T)\right\rangle + i\int_0^T d\tau\,\langle(i\partial_\tau - \mathcal{H}(\tau)\chi(\tau)|\delta\Psi(\tau)\rangle \\ - \langle\chi(T)|\delta\Psi(T)\rangle + \underbrace{\langle\chi(0)|\delta\Psi(0)\rangle}_{=0}.\end{aligned} \tag{4.11}$$

The last term vanishes since the initial condition for the wave function is fixed.

Variation with respect to the Lagrange multiplier

The variations of the first two functional expressions vanish since only J_3 depends on Lagrange multiplier χ. Therefore the variation yields

$$\delta_\chi J = -i\int_0^T d\tau\,\langle(i\partial_\tau - \mathcal{H}(\tau))\Psi(\tau)|\delta\chi(\tau)\rangle\,. \tag{4.12}$$

Variation with respect to the field

For the last independent variable, f, the first functional vanishes. The variations of the two other functional expressions are obtained as follows:

$$\delta J_2 = -\int_0^T 2\alpha f(t)\delta f(t)dt \tag{4.13}$$

$$J_3 = -2\,\mathrm{Im}\int_0^T \langle\chi(t)|(i\partial_t - \mathcal{H}_0 + g(\mathbf{r})f(t))|\Psi(t)\rangle\, dt \Rightarrow$$

$$\delta J_3 = -2\,\mathrm{Im}\int_0^T \langle\chi(t)|g(\mathbf{r})\delta f(t)|\Psi(t)\rangle\, dt. \tag{4.14}$$

By summing up δJ_2 and δJ_3, the variation of the Lagrange functional with respect to the field is found to be:

$$\delta_f J = \int_0^T d\tau\,[-2\,\mathrm{Im}\,\langle\chi(\tau)|g(\mathbf{r})|\Psi(\tau)\rangle - 2\alpha f(\tau)]\,\delta f(\tau). \tag{4.15}$$

Control equations

The criteria of finding the maximum of J correspond to setting (4.11), (4.12), and (4.15) must equal to zero. This leads to the following set of equations:

$$\alpha f(t) = -\mathrm{Im}\,\langle\chi(t)|g(\mathbf{r})|\Psi(t)\rangle\,; \tag{4.16}$$

$$(i\partial_t - \mathcal{H}(t))\Psi(\mathbf{r},t) = 0, \quad \Psi(\mathbf{r},0) = \Phi(\mathbf{r}); \tag{4.17}$$

$$\left\langle \hat{O}^\dagger\Psi(T) - \chi(T)\middle|\delta\Psi(T)\right\rangle = -i\int_0^T d\tau\,\langle(i\partial_\tau - \mathcal{H}(\tau))\chi(\tau)|\delta\Psi(\tau)\rangle\,. \tag{4.18}$$

The first equation, given the wave function and the Lagrange multiplier at a specific instant of time, gives the value of the control field at the given time. The second equation is simply the time-dependent Schödinger equation, where the initial condition is fixed, that is, $\Psi(0) = \Phi$.

The third equation needs further modification as it is quite complicated in its current form. Rewriting the left-hand side of Eq. (4.18) in an integral form yields

$$\int_0^T d\tau \left\langle \delta(\tau - T)\left(\hat{O}^\dagger \Psi(\tau) - \chi(\tau)\right) \middle| \delta\Psi(\tau) \right\rangle = -i \int_0^T d\tau \left\langle (i\partial_\tau - \mathcal{H}(\tau))\chi(\tau) | \delta\Psi(\tau) \right\rangle ;$$
$$\int_0^T d\tau \left\langle i\delta(\tau - T)\left(\hat{O}^\dagger \Psi(\tau) - \chi(\tau)\right) - (i\partial_\tau - \mathcal{H}(\tau))\chi(\tau) \middle| \delta\Psi(\tau) \right\rangle = 0. \quad (4.19)$$

Splitting the integral into two intervals yields

$$\lim_{\zeta \to 0} \int_0^{T-\zeta} d\tau \left\langle i\delta(\tau - T)\left(\hat{O}^\dagger \Psi(\tau) - \chi(\tau)\right) - (i\partial_\tau - \mathcal{H}(\tau))\chi(\tau) \middle| \delta\Psi(\tau) \right\rangle +$$
$$\int_{T-\zeta}^{T+\zeta} d\tau \left\langle i\delta(\tau - T)\left(\hat{O}^\dagger \Psi(\tau) - \chi(\tau)\right) - (i\partial_\tau - \mathcal{H}(\tau))\chi(\tau) \middle| \delta\Psi(\tau) \right\rangle = 0. \quad (4.20)$$

In the first line of Eq. (4.20), the first integrand vanishes due to the presence of the Dirac delta function. In the second line, the second term of the integrand vanishes since it is a continuous function. This leads to a set of two equations:

$$(i\partial_t - \mathcal{H}(t))|\chi(t)\rangle = 0, \quad (4.21)$$
$$|\chi(T)\rangle = \hat{O}|\Psi(T)\rangle. \quad (4.22)$$

It is worth mentioning that in the derivation the Eq. (4.22), the continuity of the Lagrange multiplier is implicitly assumed. Otherwise the integral in Eq. (4.19) has to be solved with special care.

The expressions 4.16, 4.17, 4.21, and 4.22 together form a set of equations known as *control equations*.

4.2 Algorithm

To solve the control equations, there are many algorithms such as those proposed by Zhu-Botina-Rabitz [103] and Zhu-Rabitz [104]. In those schemes the equations are solved iteratively in a forward-backward manner.

The overall view of such algorithms is such that first, with an initial guess for the field, the wave function is propagated. Afterwards, the Lagrange multiplier is found at the end of the interaction. Thereafter, the Lagrange multiplier is propagated

backward with the updated field by an infinitesimal time step. In this way, the total profile of the updated field is achieved once the Lagrange multiplier reaches the initial time step. This procedure is done once the yield reaches a certain threshold with respect to the desired final state.

Splitting this general description properly into three main parts reveals a clear picture of the procedure. Consider the first iteration, and the initial guessed field is denoted by $f^{(0)}(t)$ (correspondingly $f^{(k)}(t)$ for the k_{th} iteration). The wave function of the initial state $\Phi = \Psi^{(0)}(0)$ is propagated with the proposed field:

$$\Psi^{(0)}(0) \xrightarrow{f^{(0)}(t)} \Psi^{(0)}(T). \tag{4.23}$$

By the means of Eq. (4.22), the Lagrange multiplier is found at time T.

In order to find the updated field $\tilde{f}^{(0)}(t)$, the Lagrange multiplier has to be propagated backward in time using Eq. (4.21). The updated field can be found through Eq. (4.16). The immediate observation is the fact that Eqs. (4.16) and (4.21) are coupled, since the Hamiltonian contains the field in itself. Therefore, the Lagrange multiplier is propagated backward in time by an infinitesimal step Δt with the field $\tilde{f}^{(0)}(T)$ which is found through Eq. (4.16). The backward propagation is carried out by the Dyson operator in the interaction representation of the Hamiltonian. This operator satisfies the properties below:

$$\begin{aligned} \mathcal{U}(t,t) &= \mathbb{1}, \\ \mathcal{U}(t,t_0) &= \mathcal{U}(t,t_1)\mathcal{U}(t_1,t_0), \\ \mathcal{U}^{-1}(t,t_0) &= \mathcal{U}(t_0,t), \end{aligned} \tag{4.24}$$

where $\mathbb{1}$ is the identity operator. In the interaction picture, the Schrödinger equation is transformed to the Schwinger-Tomonaga equation [105], which yields the expression below for the Dyson operator [106]:

$$\mathcal{U}(t,t') = \mathbb{1} - i\int_{t'}^{t} d\tau U(\mathbf{r},\tau)\mathcal{U}(\tau,t'). \tag{4.25}$$

The Dyson operator $\mathcal{U}(T, T-\Delta T)$ is obtained by the current field at $t = T$. Then its

action upon $\chi(T)$ yields $\chi(T-\Delta t)$. Then, by the means of Eq. (4.16), $\tilde{f}^{(0)}(T-\Delta t)$ is found immediately. Thereafter, the Dyson operator is updated, and this procedure goes on until the whole profile of the updated field is achieved. These steps can be summarised as follows:

$$\begin{aligned}
\text{step } 0: \quad & \Psi^{(0)}(0) \xrightarrow{f^{(0)}(t)} \Psi^{(0)}(T) \\
\text{step } k: \quad & \Psi^{(k)}(T) \xrightarrow{f^{(k)}(t)} \Psi^{(k)}(0) \\
& \hat{O}\Psi^{(k)}(T) = \chi^{(k)}(T) \xrightarrow{\tilde{f}^{(k)}(t)} \chi^{(k)}(0) \\
& \chi^{(k)}(0) \xrightarrow{\tilde{f}^{(k)}(t)} \chi^{(k)}(T) \\
& \Phi = \Psi^{(k+1)}(0) \xrightarrow{f^{(k+1)}(t)} \Psi^{(k+1)}(T)
\end{aligned} \tag{4.26}$$

This algorithm converges monotonically and has a fast convergence to the maximum of the Lagrange functional J [103].

4.3 Target operator

So far the target operator $\hat{O}$ has been considered to be a general operator. In this section, two common target operators are introduced: projection operator and local operator.

4.3.1 Projection operator

The projection operator $\hat{O} = |\Phi_F\rangle\langle\Phi_F|$ is of common use to define the Frobenius distance between the wave function $\Psi(T)$ and the target wave function Φ_F. The minimisation of this distance leads to the maximisation of functional J_1:

$$\min_{f(t)} \|\Psi(T) - \Phi_F\|^2 \;\Rightarrow\; \max J_1 = |\langle\Psi(T)|\Phi_F\rangle|^2. \tag{4.27}$$

Note that maximising J_1 is independent of an arbitrary choice of the phase of Φ_F, since the Frobenius norm remains invariant under the gauge transformation $\Phi_F \rightarrow \mathrm{e}^{i\gamma}\Phi_F$.

4.3.2 Local operator

Localisation of the wave function within a certain region of space is another common choice for the target operator. Among many special functions for localisation, Dirac delta function is prevalent. Although the precise localisation is an ideal, choosing the δ-function gives rise to the desired spatial density distribution.

Similarly to the previous case, maximising the functional J_1 is equivalent to the minimization of the Frobenius norm of the target density ρ_f and density distribution $\rho(T)$:

$$\min_{f(t)} \|\sqrt{\rho(T)} - \sqrt{\rho_f}\|^2 = \min_{f(t)} \left\{2 - 2\int d\mathbf{r}\sqrt{\rho(T)\rho_f}\right\}. \tag{4.28}$$

4.4 Control field constraints

In the previous section it has been mentioned that sometimes extra constraints are required to be imposed on the field, e.g., constant fluence or frequency filtering. The Werschnik-Gross algorithm [93, 107] allows us to implement such constraints on the control field. This algorithm in contrast to the Zhu-Rabitz scheme, since it does not converge monotonically, but its convergence is guaranteed if the features of the pulse are consistent.

Spectral constraints are crucial for the experimental realisation of the simulations. Restrictions on the pulse shaping in real life experiments makes it necessary to consider frequency constraints on the control field. The gigahertz regime has already been achieved and demonstrated for a conducting tip [108, 109]. Meanwhile, laser fields can reach the terahertz regime [110]. Therefore one has to bear in mind the properties which the control field has to satisfy.

The fluence of a pulse is a measure of the energy contained in it. This measure is added to the functional J_2 and the expression (4.5) is substituted by the following functional:

$$\tilde{J}_2[f] = -\alpha\left[\int_0^T f^2(t)dt - F_0\right]. \tag{4.29}$$

The first observation of this substitution is the fact that the penalty factor α is no

longer an arbitrary choice, rather a Lagrange multiplier which has to be identified through the variation of the total functional J. The predefined value F_0 keeps the fluence of the pulse constant during the iterative procedure. Therefore, another independent parameter α is introduced to the Eq. (4.7). The variation with respect to α leads to the following condition:

$$\int_0^T f^2(t)dt = F_0. \tag{4.30}$$

Inserting the control equation (4.16) into the equation above yields:

$$\frac{1}{\alpha^2}\int_0^T \Big(\mathrm{Im}\langle\chi(t)|g(\mathbf{r})|\Psi(t)\rangle\Big)^2 dt = F_0 \Rightarrow \alpha = \sqrt{\frac{\int_0^T W^2(t)dt}{F_0}}, \tag{4.31}$$

where the square root of the integrand is substituted by $W(t)$. The rest of the Lagrange functional remains unchanged. This equation can be straightforwardly inserted in the iterative procedure of Eq. (4.26). However, at the k_th step the field, $f(t)^{(k)}$ and $\tilde{f}^k(t)$ are obtained according to:

$$\tilde{f}^{(k)}(t) = -\frac{1}{\alpha^{(k)}}\mathrm{Im}\langle\chi^{(k)}(t)|g(\mathbf{r})|\Psi^{(k)}(t)\rangle, \tag{4.32}$$

$$f^{(k+1)}(t) = \frac{\alpha^{(k)}}{\alpha^{(k+1)}}\tilde{f}^{(k)}(t). \tag{4.33}$$

At each iteration the Lagrange multiplier $\alpha^{(k+1)}$ is given by

$$\alpha^{(k+1)} = \sqrt{\frac{\int_0^T \Big(\alpha^{(k)}\tilde{f}^{(k)}(t)\Big)^2 dt}{F_0}}, \tag{4.34}$$

where the initial conditions are the same as mentioned within the previous algorithm. For the zeroth iteration $\alpha^{(0)}$ is defined as

$$\alpha^{(0)} = \sqrt{\frac{\int_0^T \left(\tilde{f}^{(0)}(t)\right)^2 dt}{F_0}}. \tag{4.35}$$

The difference between the Werschnik-Gross algorithm and the Zhu-Rabitz algorithm is that in the latter one, the control equation (4.16) is applied to control pulses $f(t)$ and $\tilde{f}(t)$ interchangeably after each forward-backward propagation, while in the former one, the control equation is only applied to $\tilde{f}(t)$ once in each forward-backward propagation. Therefore the monotonic convergence is not guaranteed in the Werschnik-Gross algorithm.

The theoretical framework developed in this chapter is used through the rest of this text to find the optimised pulse. QOCT based on the variational principle at first sight seems to be too complicated. This could easily imply confusion to catch the essentials of the dynamical behaviour of a quantum system. This is true up to some degree, but it should not be underestimated that this method contains the full dynamics of the system. Hence, the whole information of the dynamics can be extracted. Another rich advantage of this approach is that the variational method is robust against infinitesimal fluctuations introduced to the parameters of the system. In other words, one does not expect large variations on the outcomes if the parameters are slightly changed.

It is believed by the author that there exists an algorithm which could be utilised in a general optimal control problem. The method is known as the *matrix-product state representation*, and it is widely used in quantum information and computing community. In that method, the ground state of a many-body system, represented by a pure state, can be written as a hierarchy of matrix multiplications. The matrices contain the whole information of the system which is carried by the wave function of the system. After rewriting the state of the system in a matrix-product state representation, one observes that not all the matrices are full rank (this is valid if the system is not in a maximally entangled state). Therefore, by removing the unnecessary information, the essential parts of the dynamics can be captured which saves considerable amount of memory. This is the essential difference between the method and the methods already discussed in this chapter. A full description of the matrix-product state representation is given in Appendix B.

5. MODELLING AND RESULTS

The aim of this thesis is to study the controllability of QCA. For the very first step, only one electron is considered, although in the literature QCA cells consisting of two electrons have been considered [111, 112]. To pave the way for the study of QCA cells, two different cases are considered. The first one is an array of QDs positioned on a straight line, corresponding to a chain of QDs ($1 \times N$ cell). This is the simplest case, mostly considered for understanding the behaviour of the system upon the action of an external local voltage gate. The second case corresponds to an arrangement of QDs on a $2 \times N$ simple square lattice. These two cases give an overall view about the size limit of the system, which the local voltage gate(s) with specific pulse parameters could bring into the system under control. In the latter case, in the presence of the horizontal symmetry axis, two local voltage gates are considered whilst in the former case only one local voltage gate is used.

In the following sections each case is explained separately with their properties. In advance, the modelling of the system and the methodology under consideration are described. The very last section is dedicated to the case of QCA cells as a special case of a $2 \times N$ cell. For this specific cell, it will be explained how symmetry properties reduce the number of the voltage gates required for controlling the cell.

5.1 System and methodology

Generally, the Hamiltonian of an electron in a QCA structure under the action of a local voltage gate, in effective atomic units (a.u.), is given by the following expression:

$$\mathcal{H}(x, y, t) = \frac{\hat{\mathcal{P}}^2}{2} + V_c(x, y) + U(x, y, t), \tag{5.1}$$

where V_c is the confinement potential of the QD lattice and U is the local voltage gate potential. The lattice consists of $(M \times N)$ QDs, where M and N are natural numbers. The shape of the QDs is a 2D cavity potential which is described by the

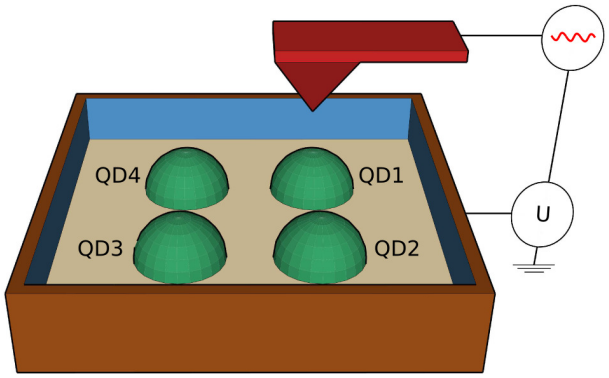

Figure 5.1 *Schematic view of 2×2 (primary unit cell) QCA. The QCA is coupled to an external voltage gate which acts locally upon the cell (here on the upper right quantum dot (QD1). The green blobs do not correspond to the quantum dot geometry but represent the electron charge density distribution.*

Fermi function. Thus the confinement potential is given as follows:

$$V_c(x,y) = -\max\left\{\frac{1}{e^{\left[\sqrt{(x-i\,a)^2+(y-j\,a)^2}-R\right]/\xi}+1} : 0 \le i \le M,\, 0 \le j \le N\right\}. \quad (5.2)$$

In this expression, $a = 6$ a.u. is the lattice constant (the distance between the centres of the two neighbour QDs), $R = 2$ a.u. is the effective radius of the QDs, and ξ is the softness parameter of the well boundary. The choice of this parameter depends on the radius of the quantum dots and the lattice constant in such a way that the effective region of each quantum dot does not overlap with its neighbours. Hence, regarding the chosen values for R and a, the softness parameter is set to $\xi = 0.21$ a.u. The material considered in this study is GaAs with the effective mass $m^* = 0.067m_0$ and the dielectric constant $\epsilon = 12.7\epsilon_0$. Therefore the energy, length, and time scale as

$$\begin{aligned} E_h^* &= (m^*/m_0)/(\epsilon/\epsilon_0)^2 E_h \approx 11 \text{ meV}, \\ a_0^* &= (\epsilon/\epsilon_0)/(m^*/m_0) a_0 \approx 10 \text{ nm}, \\ t_0^* &= \hbar/E_h^* \approx 58 \text{ fs}, \end{aligned} \quad (5.3)$$

respectively. Consequently, with this set of units, the radii of the quantum dots are around 20 nm and the lattice constant is about 60 nm. The schematic view of the system configuration for a 2×2 QCA cell is given in Fig. 5.1.

The external control agent, the local voltage gate, has to satisfy the condition that its spatial and time-dependent parts are separable. Therefore the last term in the Hamiltonian is written as follows:

$$U(x, y, t) = g(x, y)f(t), \tag{5.4}$$

where the spatial part is modelled by a Gaussian distribution below:

$$g(x, y) = \frac{\beta}{\sigma\sqrt{2\pi}} \exp\Big\{ \left[-(x - x_0)^2 - (y - y_0)^2\right] / (2\sigma^2) \Big\}. \tag{5.5}$$

We set $\sigma = 1.6$ a.u. to cover the area of a single QD at the maximum amplitude of the field and the parameter β is set to 16.04 a.u.. The proposed Gaussian shape of the conducting tip has an experimental realisation which has been already reported in Refs. [108, 109].

The *initial* guess of the time-dependent part of the voltage gate is a simple sinusoidal pulse given by $f(t) = A\sin(\omega t)$ with a frequency of $\omega = 0.001$ a.u. and an amplitude of $A = 1$ a.u. The pulse duration is set to 400 a.u., which corresponds to about 23 ps. The penalty factor is independent of time, and the fluence is kept constant during the simulation.

Since the goal is to localise the charge distribution within a specific QD, the control equations need to be rewritten in a way to suit with the proposed model. The only control equation which needs to be modified is Eq. (4.22) due to the explicit definition of the target operator. To obtain the desired output, the target operator is defined as a Heaviside distribution function multiplied by the position projection operator. Through this choice we can localise the electron in a certain region of space. Consequently, the control equations become

$$i\partial_t|\Psi(t)\rangle = \mathcal{H}(\mathbf{r}, t)|\Psi(t)\rangle, \quad |\Psi(0)\rangle = |\Phi_I\rangle, \tag{5.6a}$$

$$i\partial_t|\chi(t)\rangle = \mathcal{H}(\mathbf{r}, t)|\chi(t)\rangle, \tag{5.6b}$$

$$|\chi(T)\rangle = \Theta(|\mathbf{r} - \mathbf{r_0}|)|\mathbf{r}\rangle\langle\mathbf{r}|\Psi(T)\rangle, \tag{5.6c}$$

$$f(t) = -\frac{1}{\alpha}\langle\chi(t)|g(\mathbf{r})|\Psi(t)\rangle. \tag{5.6d}$$

Here T is the duration of the pulse and Φ_I is the initial state. The initial state is always considered to be the ground state. The expression for the two-dimensional circular Heaviside function is given by $\Theta\{-[(x-x_T)^2+(y-y_T)^2]^{1/2}+(R+1)\}$ where the tuple $\{x_T, y_T\}$ is the centre of the target quantum dot. The radius of the target is 1 a.u. larger than the radius of the quantum dot defined in Eq. (5.2).

Since a frequency filtering on the pulse is used during the optimisation, the Werschnik-Gross [107] algorithm is used for iterative forward-backward propagation of the time-dependent Schrödinger equation. The increments for real-space and time steps are $\Delta x = 0.25$ and $\Delta t = 0.0075$ a.u., respectively. The choice of these values is based on the results of the priori convergence tests. For the Dyson operator (previously introduced in Ch. 4 Sec. 2), for the infinitesimal propagation, the exponential midpoint approximation is used [113]. This explains the reason of such a small time step as the error for this approximation is of the order of $\mathcal{O}(\Delta t^2)$. For the expansion of the infinitesimal time generator, the standard approach known as symmetric splitting (Strang splitting, Marchuk splitting or Trotter splitting are the other naming conventions) is used. For further details of the algorithm, Ref. [114] is recommended for interested readers. The size of the computational box varies depending on the number of QDs. For the $1 \times N$ case, along the x-axis, a step function boundary is located at a distance a from the nearest QD centre. Along the y-axis the boundary is located at the distance $2a/3$. In the $2 \times N$ case the boundary is set along the both axes at a distance a from the centre of the nearest QD. All the calculations has been done with the OCTOPUS code published under the GPL license [115–117].

5.2 Results

5.2.1 $1 \times N$ cells

This structure corresponds to a chain of quantum dots [118, 119]. Without loss of generality, the 1×6 cell structure is considered and demonstrated in Fig. 5.2. In Fig. 5.5 the dependence of the *yield* on the number of QDs is illustrated. After the initiation of the system in its ground state, the system is subjected to a local voltage gate U, positioned on the leftmost QD, to localise the electron density distribution within the rightmost target QD denoted by 'T'. The initial field is given by Eqs. (5.4) and (5.5) with parameters β , ω, σ, and A; The fluence is 18.763 a.u. with the given parameters. The initial yield is found to be only 10%. Whilst keeping the fluenec constant as a constraint, the yield increases gradually (not monotonically) to a remarkable yield of 91.4% in the QOCT process. This is yet satisfactory for

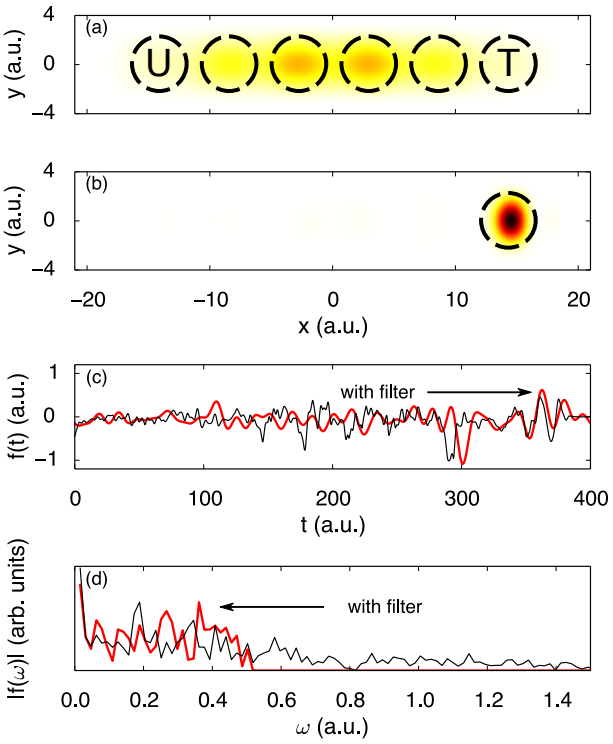

Figure 5.2 *(a) Ground state charge density distribution of the* 1×6 *cell. The approximated position of QDs is shown by black dashed circles. The local voltage gate acts on the leftmost quantum dot denoted by U and the pulse is optimised iteratively by the QOCT procedure. (b) The optimised pulse localises the charge density distribution within the rightmost QD. The profile of the optimised pulse (black thin line) is shown in (c). In order to avoid high frequency excitations, a threshold frequency of* $\omega_{th} = 0.5$ *a.u. is applied on the optimised pulse. The smoothed filtered pulse is shown by a thick red line. In (d) the Fourier spectrum with the same colouring of the optimised pulse and the filtered pulse is shown.*

such a number of QDs. The localised electron density distribution can be clearly seen in Fig. 5.2(b).

As one could expect, the pulse shape which leads to such a high yield, possesses a rather complicated pattern. This a is a consequence of the role of transitions to excited states which gives rise to many high peak frequencies in the Fourier transform of the pulse [Fig. 5.2(d)]. The pulse clearly surpasses the experimental limits in pulse shaping. Also producing such high frequencies for a voltage gate is a technical challenge yet to be reached. In order to decrease the complexity of the pulse, a frequency filter constraint is imposed on the pulse. A frequency threshold $\omega_{th} = 0.5$ a.u. is set to remove the higher frequencies from the frequency spectrum. This constraint decreases the yield to 84.7%, which is still considerable. However, the threshold frequency corresponds to 8.6 THz, which is still quite high.

The controllability is not restricted only to the rightmost QD. The calculations show that the localisation can be achieved within any QD regardless of its position on the lattice. This implies that the electron can be moved through the lattice in a desired fashion.

The convergence performance of the OCT procedure is depicted in Fig. 5.3. The non-monotonic behaviour of the convergence curve is related to the nature of the Werschnick-Gross algorithm which has already been discussed in the previous chapter. The benefit of this algorithm is the fact that in several cases it is much

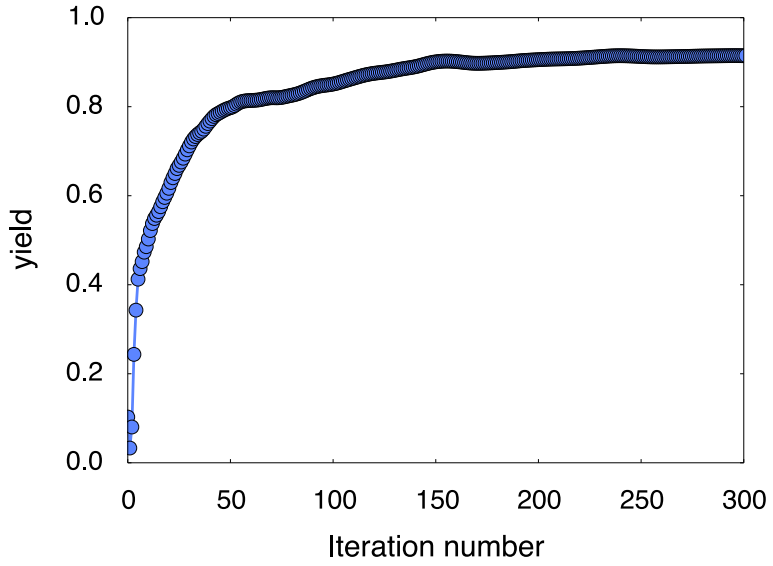

Figure 5.3 *Convergence of a quantum optimal control procedure for a* 1×6 *QCA. It can be observed that the convergence is not monotonic.*

faster in comparison with the procedure of Zhu and Rabitz.

5.2.2 $2 \times N$ cells

These cells form a realistic class of QCA structures. Especially the 2×2 cell coincides with the primary QCA cell. This cell will be explored in more detail in a separate section. A 2×2 cell owns extra symmetry properties which decrease the degrees of the freedom of the system. All these cells carry the mirror symmetry along the x-axis. The consequence of this property is the fact that that in favour of controlling the system, using two voltage gates is necessary. Furthermore, as the size of the lattice increases, the outcome of the yield is not satisfactory with only one voltage gate. Therefore, two voltage gates U_1 and U_2, positioned on the left top and left bottom QDs, are utilised and the target QD is the rightmost top one (Fig. 5.4). Again without any loss of generality, a 2×5 cell structure can be considered. The initial guess for the pulses of the two voltage gates is the same as in the previous case. Initially the yield is found to be only 2.5%, and after the optimisation procedure it increases to 94.2%. The fluence of the pulse is kept constant and corresponds to 18.763 a.u. Similarly to the previous case, a threshold frequency filter is applied on the both voltage gates, which decreases the yield to 87.6%. The corresponding pulse shapes and their Fourier spectra are illustrated in Figs 5.4(c-f).

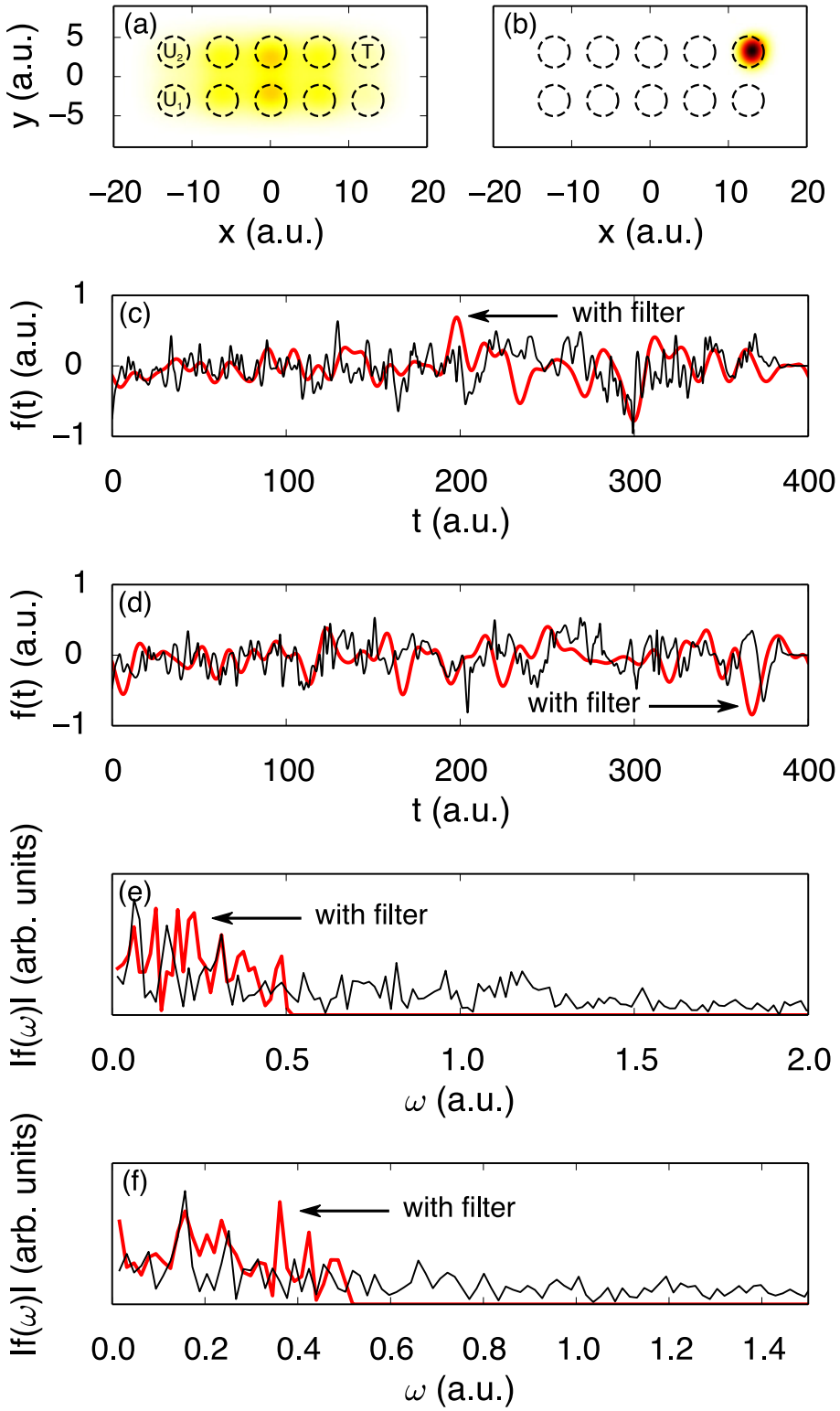

Figure 5.4 *(a) Ground state charge density distribution and (b) the localised charge density. Due to the presence of a horizontal symmetry axis, two voltage gates U_1 and U_2 are used. The target T is set on the upper-right QD. The profile of the optimised pulse and the filtered pulse ($\omega_{th} = 0.5$a.u.) for both voltage gates are illustrated in (c) and (d) respectively. The Fourier spectra are shown in (d) and (e). Regardless of the position of the target quantum dot, the yield was found to be as high as in the case considered here.*

5.2.3 Yield dependence on the lattice size and threshold frequency

Intuitively, by increasing the size of the lattice the yield would decrease monotonically. This could be justified by the calculations carried out for different lattice sizes. In Fig. 5.5(a), for $N > 6$, the yields drops faster in both cases. But one has to bear in mind that the system under study consists of only one electron. It could be expected that for more electrons, the presence of correlation and entanglement between the electrons and the underlying geometry of the lattice may produce an irregular trend in Fig. 5.5(a).

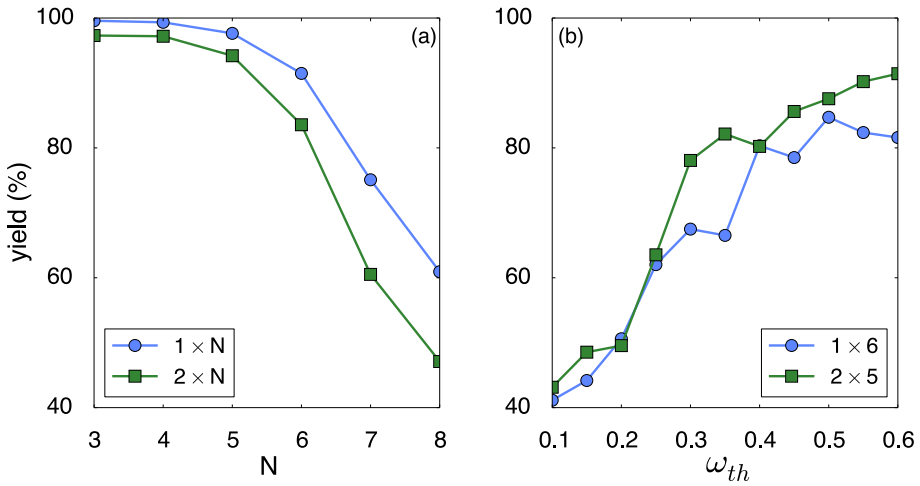

Figure 5.5 *(a) Dependence of the maximum yield for different cell sizes for both cases* $1 \times N$ *(circles) and* $2 \times N$ *(squares) systems. (b) The dependence of the maximum yield on the maximum allowed frequency* (ω_{th}) *for the optimised pulse in cases* 1×6 *(circles) and* 2×5 *(squares).*

The dependence of the yield on the threshold frequency ω_{th} on the other hand, even in these simple cases, could behave irregularly. The reason is due to the fact that the OCT procedure is a local maximisation solution. Therefore correlation between different frequencies is quite important for a global optimisation solution. Nevertheless, in Fig. 5.5(b) the trend ends at a saturation level and the best yield can be found by removing the frequency filtering completely.

5.2.4 Special case of the 2×2 cell

The case of a $2 \times N$ structure is the building block of QCA. The symmetrical properties of such a cell makes it suitable for the realisation of digits 0 and 1. For the purpose of logical computation, it is necessary to have a correspondence between the two binary digits 0 and 1 with the two distinguishable states of the QCA cell.

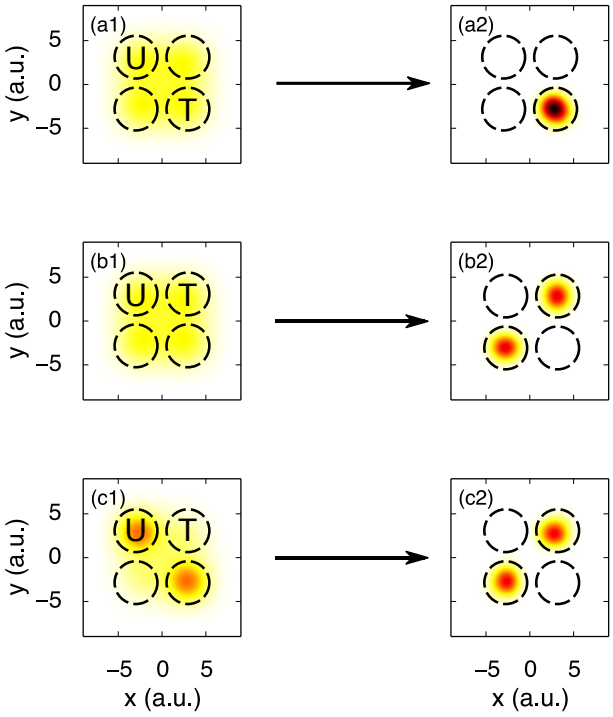

Figure 5.6 *(a) Localisation of the charge density distribution in the lower-right QD. (b) After the change of the target to the upper right QD, the optimised field yields an equally distributed charge density within anti-diagonal QDs. This corresponds to bit 1. (c) An offset is introduced to the diagonal QDs to initialise the QCA cell in bit 0. The optimised field changes the bit from 0 to 1.*

Due to the presence of the $\pi/2$ symmetry of the cell, it is a proper choice to make the diagonal and antidiagonal charge distributions correspond to digits 0 and 1, respectively.

The system is prepared in its ground state charge distribution. The QCA cell is acted by only one gate positioned on the upper-left QD. Two different target QDs are considered, one is the lower-right corner and the other one is the upper-right corner. In the first case, since the target QD is distinguishable from its upper and left QDs, the localisation would be achieved successfully [Fig. 5.6(a)]. In the latter case, the charge localisation in the upper-right QD, on the other hand, would yield an equal charge distribution in aforementioned QDs [Fig. 5.6(b)]. These two QDs are rotationally indistinguishable with respect to the point where the voltage gate is positioned. This leads to an anti-diagonal charge distribution which corresponds to the bit 1. The same procedure can be done by changing the position of the voltage gate to the upper-right QD and set the target on the upper left QD. In this situation the charge distribution will be equally distributed in diagonal QDs, corresponding to bit 0. Although these two states are the degenerate excited states of the QCA cell, introducing an offset to the diagonal QDs initialises the ground state of the system in a state corresponding to bit 0. The yield of the transition from bit 0 to 1 is found to be $>98\%$ with the same field parameters introduced earlier.

One has to note that the transition from the excited state to the ground state for only one QCA cell is not of importance but rather the global ground state of the

system of QCA cells. For clarification, being in an excited state of a QCA cell does not imply a global excited state of a system that consists of many QCA cells, see Fig. 3.9(c). This is a critical architectural design when we think of the construction of a logical gate.

6. CONCLUSIONS

What has been shown above, is the controllability of the charge distribution in single-electron quantum dot lattices. This is achieved within the framework of quantum optimal control theory and utilising a local voltage gate as an external agent. The iterative scheme for optimising the control field improves the yield significantly to as high as >90% in both cases of a chain of quantum dots ($1 \times N$) and a quantum dot cellular automaton with two coupled parallel chains of quantum dots ($2 \times N$).

Although the limit of the lattice size and the field strength are tightly related, a reasonable controllability is reachable for the pulse parameters mentioned in the text. Also, the frequency filtering constraint potentially decreases the yield. But this constraint is non-avoidable since the complex pulse shaping still is a technological challenge. Even with the laboratory tools nowadays, a terahertz regime has barely been touched.

The critical parameters which have to be considered are the frequency, pulse durations, and the amplitude of the field. Also the focusing of the conducting tip is as crucial as the other parameters. What can be concluded from the results is that a pulse with a duration of picoseconds and a remarkably high focus is still on a path to be discovered. In Refs. [108, 109] a moveable voltage gate operating in the gigahertz regime has already been demonstrated as a real experimental setup. Besides this obstacle, progress in the fabrication of quantum dot lattices is still to be expected in near future.

This study, however, sheds light on the controllability of quantum dot cellular automata cells, which is important for their future implementation in nanoscale logical gates. As it has already been mentioned, from the computational point of view, any logical gate has a realisation based on majority gates. Universal majority gates of NAND makes it possible to construct any other logical gate based on the universal gate of NAND [120, 121].

Another achievement of this study is to show that a QCA cell can be constructed with only one electron [122] in contrast to the previous convention of a two-electron

QCA cell. This decreases the physical complexity of the system considerably as we omit the electron-electron interactions in the QCA cell.

Further steps to be taken in the future are to consider a quantum dot cellular automata logical gate and the study of the controllability and its logical operation. In such systems, also controlling the coupling strength between the quantum dot cellular automata cells has to be considered as control parameters in control equations. This control parameter will set a criterion on the tunnelling phenomena which, is crucial in designing a suitable architecture for logical gates.

BIBLIOGRAPHY

[1] Mark Vogelsberger et al. Properties of galaxies reproduced by a hydrodynamic simulation. *Nature*, 509(7499):177–182, 2014.

[2] G.E. Moore. Cramming more components onto integrated circuits. *Proceedings of the IEEE*, 86(1):82–85, Jan 1998.

[3] John Von Neumann. *Theory of Self-Reproducing Automata*. University of Illinois Press, Champaign, IL, USA, 1966.

[4] Umberto Pesavento. An implementation of von Neumann's self-reproducing machine. *Artificial Life*, 2(4):337–354, 1995.

[5] Martin Gardner, Martin Gardner, Martin Gardner, and Martin Gardner. *Wheels, life, and other mathematical amusements*, volume 86. WH Freeman New York, 1983.

[6] E.R. Berlekamp, J.H. Conway, and R.K. Guy. *Winning Ways for Your Mathematical Plays*. Number v. 2. Taylor & Francis, 2003.

[7] Michael Creutz. Deterministic Ising dynamics. *Annals of Physics*, 167(1):62 – 72, 1986.

[8] Donald R. Franceschetti, D. Wayne Jones, Bruce W. Campbell, and John W. Hanneken. Hamming sets, Ising sets, cellular automata, neural nets, and the random walk. *American Journal of Physics*, 61(1):50–53, 1993.

[9] Hudong Chen, Shiyi Chen, Gary Doolen, and YC Lee. Simple lattice gas models for waves. *Complex Systems*, 2:259–267, 1988.

[10] Denise Kirschner and John Carl Panetta. Modeling immunotherapy of the tumor–immune interaction. *Journal of Mathematical Biology*, 37(3):235–252, 1998.

[11] Daniel G Mallet and Lisette G De Pillis. A cellular automata model of tumor–immune system interactions. *Journal of Theoretical Biology*, 239(3):334–350, 2006.

[12] Fei Yan, Xia-Ting Feng, Peng-Zhi Pan, and Shao-Jun Li. Discontinuous cellular automaton method for crack growth analysis without remeshing. *Applied Mathematical Modelling*, 38(1):291–307, 2014.

[13] Pece V Gorsevski, Charles M Onasch, John R Farver, and Xinyue Ye. Detecting grain boundaries in deformed rocks using a cellular automata approach. *Computers & Geosciences*, 42:136–142, 2012.

[14] Daniel C Dennett. Real patterns. *The Journal of Philosophy*, pages 27–51, 1991.

[15] Edward Fredkin. *A new cosmogony*. Department of Physics, Boston University, 1992.

[16] Stephan Foldes. *Fundamental structures of algebra and discrete mathematics*. John Wiley & Sons, 2011.

[17] Wolfram science group. `http://atlas.wolfram.com`.

[18] D. Beauquier and M. Nivat. On translating one polyomino to tile the plane. *Discrete and & Computational Geometry*, 6(1):575–592, 1991.

[19] Andrew Ilachinski. Cellular automata–a discrete universe. *Kybernetes*, 32(4), 2003.

[20] Stephen Wolfram. Statistical mechanics of cellular automata. *Review of Modern Physics*, 55:601–644, Jul 1983.

[21] Alan Mathison Turing. On computable numbers, with an application to the entscheidungsproblem. *Journal of Mathematics*, 58:345–363, 1936.

[22] Martin Davis. *Computability & unsolvability*. Courier Dover Publications, 1982.

[23] Norman H Packard. *Adaptation toward the edge of chaos*. University of Illinois at Urbana-Champaign, Center for Complex Systems Research, 1988.

[24] Chris G Langton. Computation at the edge of chaos: phase transitions and emergent computation. *Physica D: Nonlinear Phenomena*, 42(1):12–37, 1990.

[25] M. Mitchell, P. T. Mitchell, and J. P. Crutchfield. Revisiting the edge of chaos: Evolving cellular automata to perform computations. *Complex Systems*, 7(2):89–130, 1993.

[26] JP Crutchfield and K Young. *Computation at the onset of chaos, complexity, entropy and the physics of information (Redwood City)(Zurek, W. H. Ed.)*. Addison-Wesley, 1990.

[27] Tommaso Toffoli and Norman Margolus. *Cellular automata machines: a new environment for modeling*. MIT Press, 1987.

[28] Marc A Kasfner. Artificial atoms. *Physics today*, page 25, 1993.

[29] Jozef T Devreese and F Peeters. *The physics of the two-dimensional electron gas*, volume 157. Plenum Publishing Corporation, 1987.

[30] B.G. Streetman and S. Banerjee. *Solid State Electronic Devices*. Pearson Education, Limited, 2014.

[31] M. Ciorga, A. S. Sachrajda, P. Hawrylak, C. Gould, P. Zawadzki, S. Jullian, Y. Feng, and Z. Wasilewski. Addition spectrum of a lateral dot from coulomb and spin-blockade spectroscopy. *Physical Review B*, 61:R16315–R16318, Jun 2000.

[32] Thaddeus D Ladd, Fedor Jelezko, Raymond Laflamme, Yasunobu Nakamura, Christopher Monroe, and Jeremy L O'Brien. Quantum computers. *Nature*, 464(7285):45–53, 2010.

[33] Robert H. Blick and Heribert Lorenz. Possible definition of quantum bits in coupled quantum dots. In *Circuits and Systems, 2000. Proceedings. ISCAS 2000 Geneva. The 2000 IEEE International Symposium on*, volume 2, pages 245–248 vol.2, 2000.

[34] D.V. Averin and K.K. Likharev. Coulomb blockade of single-electron tunneling, and coherent oscillations in small tunnel junctions. *Journal of Low Temperature Physics*, 62(3-4):345–373, 1986.

[35] DV Averin and KK Likharev. Single electronics: A correlated transfer of single electrons and cooper pairs in systems of small tunnel junctions. *Mesoscopic Phenomena in Solids*, 30:173–271, 1991.

[36] Hermann Grabert and Michel H Devoret. Single charge tunneling: Coulomb blockade phenomena in nanostructures, nato asi series. *Physics (Plenum Press, New York, 1992)*, 1992.

[37] LeoP. Kouwenhoven, CharlesM. Marcus, PaulL. McEuen, Seigo Tarucha, RobertM. Westervelt, and NedS. Wingreen. Electron transport in quantum dots. In LydiaL. Sohn, LeoP. Kouwenhoven, and Gerd Schön, editors, *Mesoscopic Electron Transport*, volume 345 of *NATO ASI Series*, pages 105–214. Springer Netherlands, 1997.

[38] George Boole. *The mathematical analysis of logic*. Philosophical Library, 1847.

[39] Michael A Nielsen and Isaac L Chuang. *Quantum computation and quantum information*. Cambridge University Press, 2010.

[40] Guifré Vidal. Efficient classical simulation of slightly entangled quantum computations. *Physical Review Letters*, 91:147902, Oct 2003.

[41] P. Shor. Polynomial-time algorithms for prime factorization and discrete logarithms on a quantum computer. *SIAM Review*, 41(2):303–332, 1999.

[42] Charles H. Bennett and Stephen J. Wiesner. Communication via one- and two-particle operators on Einstein-Podolsky-Rosen states. *Physical Review Letters*, 69:2881–2884, Nov 1992.

[43] Charles H Bennett, Gilles Brassard, et al. Quantum cryptography: Public key distribution and coin tossing. In *Proceedings of IEEE International Conference on Computers, Systems and Signal Processing*, volume 175. New York, 1984.

[44] Nelson Dunford, Jacob T Schwartz, William G Bade, and Robert G Bartle. *Linear operators*. Wiley-Interscience New York, 1971.

[45] Nicolas Gisin. Weinberg's non-linear quantum mechanics and supraluminal communications. *Physics Letters A*, 143(1):1–2, 1990.

[46] Nicolas Gisin. Bell's inequality holds for all non-product states. *Physics Letters A*, 154(5):201–202, 1991.

[47] Joseph Polchinski. Weinberg's nonlinear quantum mechanics and the Einstein-Podolsky-Rosen paradox. *Physical Review Letters*, 66:397–400, Jan 1991.

[48] Albert Einstein, Boris Podolsky, and Nathan Rosen. Can quantum-mechanical description of physical reality be considered complete? *Physical Review*, 47(10):777, 1935.

[49] John S Bell et al. On the Einstein-Podolsky-Rosen paradox. *Physics*, 1(3):195–200, 1964.

[50] John S Bell. On the problem of hidden variables in quantum mechanics. *Reviews of Modern Physics*, 38(3):447, 1966.

[51] Steven Weinberg. *Dreams of a final theory*. Random House LLC, 1992.

[52] N Gisin and M Rigo. Relevant and irrelevant nonlinear schrodinger equations. *Journal of Physics A: Mathematical and General*, 28(24):7375, 1995.

[53] W Lücke. Nonlinear Schrödinger dynamics and nonlinear observables. *arXiv preprint quant-ph/9505022*, 1995.

[54] Bogdan Mielnik. Generalized quantum mechanics. *Communications in Mathematical Physics*, 37(3):221–256, 1974.

[55] W. van der Wiel, S. De Franceschi, J. Elzerman, T. Fujisawa, S. Tarucha, and L. Kouwenhoven. Electron transport through double quantum dots. *Review of Modern Physics*, 75:1–22, Dec 2002.

[56] M Kemerink and LW Molenkamp. Stochastic Coulomb blockade in a double quantum dot. *Applied Physics Letters*, 65(8):1012–1014, 1994.

[57] NC Van der Vaart, SF Godijn, Yu V Nazarov, CJPM Harmans, JE Mooij, LW Molenkamp, and CT Foxon. Resonant tunneling through two discrete energy states. *Physical Review Letters*, 74(23):4702, 1995.

[58] TH Oosterkamp, T Fujisawa, WG Van Der Wiel, K Ishibashi, RV Hijman, S Tarucha, and Leo P Kouwenhoven. Microwave spectroscopy of a quantum-dot molecule. *Nature*, 395(6705):873–876, 1998.

[59] Toshimasa Fujisawa, Tjerk H Oosterkamp, Wilfred G Van der Wiel, Benno W Broer, Ramón Aguado, Seigo Tarucha, and Leo P Kouwenhoven. Spontaneous emission spectrum in double quantum dot devices. *Science*, 282(5390):932–935, 1998.

[60] Heejun Jeong, Albert M Chang, and Michael R Melloch. The Kondo effect in an artificial quantum dot molecule. *Science*, 293(5538):2221–2223, 2001.

[61] F. Hofmann, T. Heinzel, D.A. Wharam, J.P. Kotthaus, G. Böhm, W. Klein, G. Tränkle, and G. Weimann. Single electron switching in a parallel quantum dot. *Physical Review B*, 51:13872–13875, May 1995.

[62] AS Adourian, C Livermore, RM Westervelt, KL Campman, and AC Gossard. Single electron charging in parallel coupled quantum dots. *Superlattices and Microstructures*, 20(3):411–417, 1996.

[63] AS Adourian, C Livermore, RM Westervelt, KL Campman, and AC Gossard. Evolution of Coulomb blockade spectra in parallel coupled quantum dots. *Applied Physics Letters*, 75(3):424–426, 1999.

[64] Mark A Reed, John N Randall, James H Luscombe, William R Frensley, Raj J Aggarwal, Richard J Matyi, Tom M Moore, and Anna E Wetsel. Quantum dot resonant tunneling spectroscopy. In *Festkörperprobleme 29*, pages 267–283. Springer, 1989.

[65] Seigo Tarucha, T Fujisawa, K Ono, DG Austing, TH Oosterkamp, WG van der Wiel, and LP Kouwenhoven. Elastic and inelastic single electron tunneling in coupled two dot system. *Microelectronic Engineering*, 47(1):101–105, 1999.

[66] S Amaha, DG Austing, Y Tokura, K Muraki, K Ono, and S Tarucha. Magnetic field induced transitions in the few-electron ground states of artificial molecules. *Solid State Communications*, 119(4):183–190, 2001.

[67] CH Crouch, C Livermore, RM Westervelt, KL Campman, and AC Gossard. Evolution of the Coulomb gap in tunnel-coupled quantum dots. *Applied Physics Letters*, 71(6):817–819, 1997.

[68] T. Stoof and Yu. Nazarov. Time-dependent resonant tunneling via two discrete states. *Physical Review B*, 53:1050–1053, Jan 1996.

[69] B. Hazelzet, M. Wegewijs, T. Stoof, and Yu. Nazarov. Coherent and incoherent pumping of electrons in double quantum dots. *Physical Review B*, 63:165313, Apr 2001.

[70] H Pothier, P Lafarge, C Urbina, D Esteve, and MH Devoret. Single-electron pump based on charging effects. *EPL (Europhysics Letters)*, 17(3):249, 1992.

[71] LD Landau and EM Lifshitz. Statistical physics, part i. *Course of Theoretical Physics*, 5:468, 1980.

[72] Toshimasa Fujisawa, Toshiaki Hayashi, HD Cheong, YH Jeong, and Yoshiro Hirayama. Rotation and phase-shift operations for a charge qubit in a double quantum dot. *Physica E: Low-dimensional Systems and Nanostructures*, 21(2):1046–1052, 2004.

[73] KD Petersson, JR Petta, H Lu, and AC Gossard. Quantum coherence in a one-electron semiconductor charge qubit. *Physical Review Letters*, 105(24):246804, 2010.

[74] L. C. L. Hollenberg, A. S. Dzurak, C. Wellard, A. R. Hamilton, D. J. Reilly, G. J. Milburn, and R. G. Clark. Charge-based quantum computing using single donors in semiconductors. *Physical Review B*, 69:113301, Mar 2004.

[75] JM Elzerman, R Hanson, LH Willems Van Beveren, B Witkamp, LMK Vandersypen, and Leo P Kouwenhoven. Single-shot read-out of an individual electron spin in a quantum dot. *Nature*, 430(6998):431–435, 2004.

[76] DJ Reilly, JM Taylor, JR Petta, CM Marcus, MP Hanson, and AC Gossard. Suppressing spin qubit dephasing by nuclear state preparation. *Science*, 321(5890):817–821, 2008.

[77] T. Hayashi, T. Fujisawa, H. D. Cheong, Y. H. Jeong, and Y. Hirayama. Coherent manipulation of electronic states in a double quantum dot. *Physical Review Letters*, 91:226804, Nov 2003.

[78] Adriano Barenco, David Deutsch, Artur Ekert, and Richard Jozsa. Conditional quantum dynamics and logic gates. *Physical Review Letters*, 74(20):4083, 1995.

[79] Géza Tóth and Craig S. Lent. Quantum computing with quantum-dot cellular automata. *Physical Review A*, 63:052315, Apr 2001.

[80] J. Millman and C.C. Halkias. *Electronic Devices and Circuits*. McGraw-HIll Books, 1988.

[81] Rolf Landauer. Irreversibility and heat generation in the computing process. *IBM Journal of Research and Development*, 5(3):183–191, 1961.

[82] Graham P Boechler, Jean M Whitney, Craig S Lent, Alexei O Orlov, and Gregory L Snider. Fundamental limits of energy dissipation in charge-based computing. *Applied Physics Letters*, 97(10):103502, 2010.

[83] GP Boechler, JM Whitney, CS Lent, AO Orlov, and GL Snider. Response to" comment on'fundamental limits of energy dissipation in charge-based computing'"[appl. phys. lett. 98, 096101 (2011)]. *Applied Physics Letters*, 98(9):096102, 2011.

[84] Alexei O Orlov, Islamshah Amlani, Geza Toth, Craig S Lent, Gary H Bernstein, and Gregory L Snider. Experimental demonstration of a binary wire for quantum-dot cellular automata. *Applied Physics Letters*, 74(19):2875–2877, 1999.

[85] Donald E Knuth. The art of computer programming. volume 4, fascicle 0. introduction to combinatorial algorithms and boolean functions, 2008.

[86] John C. Bean. Quantum-dot cellular automata (qca) - logic gates, Feb 2006.

[87] Herbert Goldstein. *Classical Mechanics*. Pearson Education India, 1957.

[88] Morris Kline. *Mathematical thought from ancient to modern times*, volume 3. Oxford University Press, 1990.

[89] Wolfgang Yourgrau. *Variational principles in dynamics and quantum theory*. Courier Corporation, 1979.

[90] Robert K Nesbet. *Variational principles and methods in theoretical physics and chemistry*. Cambridge University Press, 2002.

[91] Carl B Boyer and Uta C Merzbach. *A history of mathematics*. John Wiley & Sons, 2011.

[92] T. H. Maiman. Stimulated optical radiation in ruby. *Nature*, 187:493–494, 1960.

[93] J Werschnik and E K U Gross. Quantum optimal control theory. *Journal of Physics B: Atomic, Molecular and Optical Physics*, 40(18):R175, 2007.

[94] Herschel Rabitz, Regina de Vivie-Riedle, Marcus Motzkus, and Karl Kompa. Whither the future of controlling quantum phenomena? *Science*, 288(5467):824–828, 2000.

[95] David J. Tannor and Stuart A. Rice. Control of selectivity of chemical reaction via control of wave packet evolution. *The Journal of Chemical Physics*, 83(10):5013–5018, 1985.

[96] Paul Brumer and Moshe Shapiro. Control of unimolecular reactions using coherent light. *Chemical Physics Letters*, 126(6):541 – 546, 1986.

[97] U. Gaubatz, P. Rudecki, S. Schiemann, and K. Bergmann. Population transfer between molecular vibrational levels by stimulated raman scattering with partially overlapping laser fields. a new concept and experimental results. *The Journal of Chemical Physics*, 92(9):5363–5376, 1990.

[98] Anthony P. Peirce, Mohammed A. Dahleh, and Herschel Rabitz. Optimal control of quantum-mechanical systems: Existence, numerical approximation, and applications. *Physical Review A*, 37:4950–4964, Jun 1988.

[99] R. Kosloff, S.A. Rice, P. Gaspard, S. Tersigni, and D.J. Tannor. Wavepacket dancing: Achieving chemical selectivity by shaping light pulses. *Chemical Physics*, 139(1):201 – 220, 1989.

[100] Thomas Blasi, Mario F. Borunda, Esa Räsänen, and Eric J. Heller. Optimal local control of coherent dynamics in custom-made nanostructures. *Physical Review B*, 87:241303, Jun 2013.

[101] Karsten Sundermann and Regina de Vivie-Riedle. Extensions to quantum optimal control algorithms and applications to special problems in state selective molecular dynamics. *The Journal of Chemical Physics*, 110(4):1896–1904, 1999.

[102] LD Landau and EM Lifshitz. Classical Mechanics, 1960.

[103] Wusheng Zhu, Jair Botina, and Herschel Rabitz. Rapidly convergent iteration methods for quantum optimal control of population. *The Journal of Chemical Physics*, 108(5):1953–1963, 1998.

[104] Wusheng Zhu and Herschel Rabitz. A rapid monotonically convergent iteration algorithm for quantum optimal control over the expectation value of a positive definite operator. *The Journal of Chemical Physics*, 109(2):385–391, 1998.

[105] A. Messiah. *Quantum Mechanics*. Dover Books on Physics. Dover Publications, 1961.

[106] J.W. Negele and H. Orland. *Quantum Many-particle Systems*. Advanced Books Classics. Westview Press, 2008.

[107] J Werschnik and E K U Gross. Tailoring laser pulses with spectral and fluence constraints using optimal control theory. *Journal of Optics B: Quantum and Semiclassical Optics*, 7(10):S300, 2005.

[108] Parisa Fallahi, Ania C. Bleszynski, Robert M. Westervelt, Jian Huang, Jamie D. Walls, Eric J. Heller, Micah Hanson, and Arthur C. Gossard. Imaging a single-electron quantum dot. *Nano Letters*, 5(2):223–226, 2005.

[109] Ania C. Bleszynski-Jayich, Linus E. Fröberg, Mikael T. Björk, H. J. Trodahl, Lars Samuelson, and R. M. Westervelt. Imaging a one-electron inas quantum dot in an InAs/InP nanowire. *Physical Review B*, 77:245327, Jun 2008.

[110] Andrew M. Weiner. Ultrafast optical pulse shaping: A tutorial review. *Optics Communications*, 284(15):3669 – 3692, 2011.

[111] Wolfgang Porod. Quantum-dot devices and quantum-dot cellular automata. *International Journal of Bifurcation and Chaos*, 7(10):2199–2218, 1997.

[112] Craig S Lent and Beth Isaksen. Clocked molecular quantum-dot cellular automata. *Electron Devices, IEEE Transactions on*, 50(9):1890–1896, 2003.

[113] D Vaughan Griffiths and Ian Moffat Smith. *Numerical methods for engineers*. CRC Press, 2006.

[114] M.D Feit, J.A Fleck Jr., and A Steiger. Solution of the Schrödinger equation by a spectral method. *Journal of Computational Physics*, 47(3):412 – 433, 1982.

[115] Miguel AL Marques, Alberto Castro, George F Bertsch, and Angel Rubio. octopus: a first-principles tool for excited electron–ion dynamics. *Computer Physics Communications*, 151(1):60–78, 2003.

[116] Alberto Castro, Heiko Appel, Micael Oliveira, Carlo A. Rozzi, Xavier Andrade, Florian Lorenzen, M. A. L. Marques, E. K. U. Gross, and Angel Rubio. octopus: a tool for the application of time-dependent density functional theory. *Physica Status Solidi (b)*, 243(11):2465–2488, 2006.

[117] Xavier Andrade, Joseba Alberdi-Rodriguez, David A Strubbe, Micael JT Oliveira, Fernando Nogueira, Alberto Castro, Javier Muguerza, Agustin Arruabarrena, Steven G Louie, Alán Aspuru-Guzik, et al. Time-dependent density-functional theory in massively parallel computer architectures: the octopus project. *Journal of Physics: Condensed Matter*, 24(23):233202, 2012.

[118] M. Koskinen, S. M. Reimann, and M. Manninen. Spontaneous magnetism of quantum dot lattices. *Physical Review Letters*, 90:066802, Feb 2003.

[119] A. Castro, E. Räsänen, and C. A. Rozzi. Exact coulomb cutoff technique for supercell calculations in two dimensions. *Physical Review B*, 80:033102, Jul 2009.

[120] Herbert Enderton and Herbert B Enderton. *A mathematical introduction to logic*. Academic Press, 2001.

[121] Alexis De Vos. *Reversible computing: fundamentals, quantum computing, and applications*. John Wiley & Sons, 2011.

[122] Yousof Mardoukhi and Esa Räsänen. Optimal control of charge with local gates in quantum-dot lattices. *The European Physical Journal B*, 87(6), 2014.

[123] David Perez-Garcia, Frank Verstraete, Michael M Wolf, and J Ignacio Cirac. Matrix product state representations. *arXiv preprint quant-ph/0608197*, 2006.

[124] M. Fannes, B. Nachtergaele, and R.F. Werner. Finitely correlated states on quantum spin chains. *Communications in Mathematical Physics*, 144(3):443–490, 1992.

[125] Hamed Saberi, Andreas Weichselbaum, and Jan von Delft. Matrix-product-state comparison of the numerical renormalization group and the variational formulation of the density-matrix renormalization group. *Physical Review B*, 78:035124, Jul 2008.

[126] A. Weichselbaum, F. Verstraete, U. Schollwöck, J. I. Cirac, and Jan von Delft. Variational matrix-product-state approach to quantum impurity models. *Physical Review B*, 80:165117, Oct 2009.

[127] Iztok Pižorn and Frank Verstraete. Variational numerical renormalization group: Bridging the gap between nrg and density matrix renormalization group. *Physical Review Letters*, 108:067202, Feb 2012.

[128] Christian Schön. *Quantum Information Processing and Cavity QED*. PhD thesis, Universität München, 2005.

[129] C. Schön, E. Solano, F. Verstraete, J. I. Cirac, and M. M. Wolf. Sequential generation of entangled multiqubit states. *Physical Review Letters*, 95:110503, Sep 2005.

[130] Y. Delgado, L. Lamata, J. León, D. Salgado, and E. Solano. Sequential quantum cloning. *Physical Review Letters*, 98:150502, Apr 2007.

[131] Dimitri P Bertsekas. Constrained optimization and lagrange multiplier methods. *Computer Science and Applied Mathematics, Boston: Academic Press, 1982*, 1, 1982.

[132] Hamed Saberi and Yousof Mardoukhi. Sequential quantum cloning under real-life conditions. *Physical Review A*, 85:052323, May 2012.

[133] Stefan Rommer and Stellan Östlund. Class of ansatz wave functions for one-dimensional spin systems and their relation to the density matrix renormalization group. *Physical Review B*, 55:2164–2181, Jan 1997.

[134] A Klumper, A Schadschneider, and J Zittartz. Equivalence and solution of anisotropic spin-1 models and generalized t-j fermion models in one dimension. *Journal of Physics A: Mathematical and General*, 24(16):L955, 1991.

[135] F. Verstraete and J. I. Cirac. Valence-bond states for quantum computation. *Physical Review A*, 70:060302, Dec 2004.

[136] Hamed Saberi. *Matrix-product states for strongly correlated systems and quantum information processing*. PhD thesis, Ludwig-Maximilians-Universität München, 2009.

[137] RV Mishmash and LD Carr. Ultracold atoms in 1d optical lattices: mean field, quantum field, computation, and soliton formation. *Mathematics and Computers in Simulation*, 80(4):732–740, 2009.

[138] Simon Sirca and Martin Horvat. *Computational methods for physicists: compendium for students*. Springer, 2012.

[139] David P DiVincenzo, Dave Bacon, Julia Kempe, Guido Burkard, and K Birgitta Whaley. Universal quantum computation with the exchange interaction. *Nature*, 408(6810):339–342, 2000.

[140] Hamed Saberi. Ancilla-assisted sequential approximation of nonlocal unitary operations. *Physical Review A*, 84:032323, Sep 2011.

[141] Frank Verstraete, Valentin Murg, and J Ignacio Cirac. Matrix product states, projected entangled pair states, and variational renormalization group methods for quantum spin systems. *Advances in Physics*, 57(2):143–224, 2008.

[142] Norbert Schuch, Ignacio Cirac, and David Pérez-García. Peps as ground states: Degeneracy and topology. *Annals of Physics*, 325(10):2153–2192, 2010.

[143] Amin Hosseinkhani, Bahareh Ghannad Dezfouli, Fatemeh Ghasemipour, Ali T. Rezakhani, and Hamed Saberi. Uncontrolled disorder effects in fabricating photonic quantum simulators on a kagome geometry: A projected-entangled-pair-state versus exact-diagonalization analysis. *Physical Review A*, 89:062324, Jun 2014.

A. APPENDIX A. MATRIX-PRODUCT STATE REPRESENTATION

In this thesis the mathematical framework which has been used for the study of the controllability of a quantum system is based on the variational principle. This method alone is not powerful enough for the study of a general system with quantum mechanical behaviour. The reason is that in a general case, the wave function of a many-body quantum system is hard to find. Therefore an approach to the control problem is to mix the variational method with other theoretical frameworks such as density-functional theory.

The number of problems which can be solved only by applying the variational method is limited to the cases where the wave function of the system can be represented by a pure state, or to systems where the entanglement of the sub-systems is weak (weakly interacting systems). Besides that, the information the wave function of the system carries exponentially grows with the increase of the degrees of freedom. This explains why some other theoretical methods such as density-functional theory is utilised to reduce the complexity of the problem.

Pérez-García, Verstraete, Wolf and Cirac have shown that a multipartite entangled state of a many-body quantum system, where the correlations between its subsystems are *local*, can be characterised in matrix-product states (MPS) representation [123]. It has first been proposed in a spin-chain model [124] and later on became a unified framework for the description of strongly correlated systems, where renormalisation group techniques are extensively in use [125–127]. The importance of *local* interactions is the fact that the ground states of such systems are not uniformly distributed over the whole Hilbert space. Therefore the MPS of such a state captures the essential properties of the system (The *local* and *non-local* paradigms have already been discussed when Bell's inequality was introduced in Ch. 3 Sec. 2). Another benefit of the MPS representation is that it is based on the already well-developed algebraic structures of the matrices, and it is tightly related to the concept of the *singular value decomposition* (SVD), which will be discussed later. Also, a p-norm can be naturally used as tool to measure the *distance* (representative

of correlations in the system) between the matrices.

Matrix-product states are widely used in quantum information and computation. It has been mentioned that in order to achieve an exponential speed-up in quantum computing, entanglement is an essential ingredient. Preparing an entangled multi-qubit by a single unitary operation is practically impossible due to the infinite number of degrees of freedom. An approach to overcome this obstacle is to *sequentially* couple the qubits. This procedure is accompanied by an external agent called *ancilla* (explanation will be given later). This class of qubits is found to be fully described by a hierarchy product of matrices [128–130]. This evidently implies a full control over all degrees of freedom. In real life, there are restrictions due to experimental limitations and not all the degrees of the freedom can be manipulated easily. Therefore the best prepared entangled state is always an approximation as a consequence of second law of thermodynamics. In order to include these restrictions, *constrained* optimisation has been used by introduction to *Lagrange multipliers* [131, 132].

Density-matrix renormalisation group simply leads to MPS. In order to clarify the relation, assume a spin-chain of n-1 sites and each site has m_s possible states. The exact treatment of the system needs m_s^{n-1} and therefore for a large n the amount of information will explode exponentially. Thus an approximation to the number of bases is made, and we further assume the existence of a basis set $\{|\beta\rangle_{n-1}\}$ with cardinality m such that $m \leq m_s^{n-1}$. By adding a new single site, the number of total sites becomes n with $m_s \times m$ states. The new basis set is generated by $\{|s_n\rangle \otimes |\beta\rangle_{n-1}\}$, where $\otimes$ denotes the tensor product and $|s_n\rangle$ is the eigenstate that corresponds to the newly added state s_n. A projection operator A_n is introduced to produce a new truncated basis set with m states. The new basis set is related to the *n-1* basis set through the relation below:

$$|\alpha\rangle_n = \sum_{\beta, s_n} A_n^{\alpha,(\beta,s_n)} |s_n\rangle| \otimes |\beta\rangle_{n-1}. \tag{A.1}$$

Matrices A_n are variational parameters of the matrix-product representation. They can be identified by the algebraic approach of SVD. The basis set $\{|\beta_{n-1}\rangle\}$ can be constructed recursively from $|\beta_0\rangle$ by fixing the boundary condition. Thus the recursive application of the renormalisation procedure for a chain of length n yields

$$|\alpha\rangle_n = \sum_{s_n, s_{n-1}, ..., s_1} \Big(A_n[s_n] A_{n-1}[s_{n-1}] ... A_1[s_1] \Big)^{\alpha,\beta} |s_n s_{n-1} ... s_1\rangle \otimes |\beta\rangle_0, \tag{A.2}$$

where $A_n^{\alpha,\beta}[s_n] \equiv A_n^{\alpha,(\beta,s_n)}$. It is obvious that the state given by the equation above is in its matrix-product representation. It is important to note that although the state α_n is the sum of the tensor product of local Hilbert spaces, the correlation information between the sites is carried by the products of the A-matrices [133].

MPS form a class of states which can be written in a matrix-product representation as in Eq. (A.2). Assume a general pure state $|\Psi\rangle \in \mathbb{C}^{\otimes d^N}$. This state is the characteristic wave function of a system with N sites, each belonging to a d-dimensional Hilbert space. This dimension is also called the local dimension of the system. Each site is virtually attached to two auxiliary sites with dimension D_k. Further we can assume that the pair states of these two auxiliary sites are initiated in a maximally entangled state $|I\rangle_k = \sum_{\alpha=1}^{D_k} |\alpha, \alpha\rangle$, where k enumerates the site. This state is commonly referred to as a entangled *bond* [123]. Thereafter, the application of the map

$$\mathcal{A}^{[k]} = \sum_{i_k=1}^{d} \sum_{\alpha_k, \beta_k=1}^{D_k} A^{[k]}_{i_k, \alpha_k, \beta_k} |i_k\rangle\langle\alpha_k, \beta_k| \tag{A.3}$$

on each of the N sites, leads to the finding the state $|\Psi\rangle$ will be identified consequently by its matrix-product representation given below:

$$|\Psi\rangle = \sum_{i_1, i_2, ..., i_N}^{d} \mathrm{tr} \left[A^{[1]}_{i_1} A^{[2]}_{i_2} ... A^{[N]}_{i_N} \right] |i_1, i_2, ..., i_N\rangle. \tag{A.4}$$

Here A_i is a rank-3 tensor with elements $A_{i_k, \alpha_k, \beta_k}$, and $A^{[k]}_{i_k}$ is a $D_k \times D_{k+1}$ matrix. This state is called a *matrix-product state* [134].

If $D \equiv \max_k D_k$ the MPS is said to have the *bond dimension* D. It has already been mentioned that any pure state of a many-body quantum system can be efficiently simulated on a classical computer, if the measure of the entanglement does not exceed a certain level. Vidal [40], has shown that these states have a MPS representation if the bond dimensions D_k are sufficiently large.

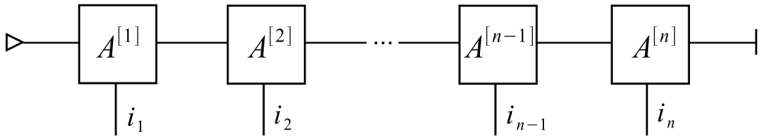

Figure A.1 *Schematic representation of the products of the A-matrices known as a valence-bond diagram. It illustrates how the contraction is carried out between the different sites [123, 135]. The reason that the indices k and k+1 are used for D is the fact that the bond dimensions of different auxiliary sites are not necessarily the same. The figure is adopted from Ref. [136].*

A MPS has an *open boundary condition* (OBC) if the first and last matrices ($A^{[1]}_{i_1}$ and $A^{[N]}_{i_N}$) are vectors. Thus, Eq. (A.4) can be simplified as follows:

$$|\psi\rangle = \sum_{i_1,i_2,...,i_N}^{d} A^{[1]}_{i_1} A^{[2]}_{i_2} ... A^{[N]}_{i_N} |i_1, i_2, ..., i_N\rangle. \tag{A.5}$$

In this equation $D_1 = D_{N+1} = 1$. Furthermore, this representation is canonical for any pure state $|\Psi\rangle \in \mathbb{C}^{\otimes d^N}$ and $D \leq d^{\lfloor d/2 \rfloor}$ if the conditions below are fulfilled [40]:

- $\sum_i A^{[m]}_i A^{[m]\dagger}_i = \mathbb{1}_{D_m}$ for all m
- $\sum_i A^{[m]\dagger}_i \Lambda^{[m-1]} A^{[m]}_i = \Lambda^{[m]}$, for all m
- $\Lambda^{[0]} = \Lambda^{[N]} = 1$, where $\Lambda^{[m]}$ is a full rank $D_{m+1} \times D_{m+1}$ matrix. It is positive definite and its trace is 1.

These conditions, known as *gauge conditions*, imply the uniqueness of the representation up to permutations and degeneracies in the Schmidt decomposition. Obtaining the A-matrices is the main objective in constructing the MPS representation of an arbitrary pure state. The whole information of the system and the interactions between the sub-systems are stored in these matrices. A general N qubit system is considered for the rest of the explanation. Now the number of local degrees of freedom is $d = 2$. The procedure is the same for systems with general local degrees of freedom d. Assume that the system consists of N sub-systems and is partitioned into two partites A and B. The whole system is described by the state given below:

$$|\Psi\rangle = c_{i_1,i_2,...,i_N} \sum_{i_1=0}^{1} ... \sum_{i_N=0}^{1} |i_1\rangle \otimes ... |i_N\rangle. \tag{A.6}$$

The Schmidt decomposition (SD) of the state $|\Psi\rangle$ reads as follows:

$$|\Psi\rangle = \sum_{\alpha=1}^{\chi_A} \lambda_\alpha |\Phi_\alpha^{[A]}\rangle \otimes |\Phi_\alpha^{[B]}\rangle. \tag{A.7}$$

Here $|\Phi_\alpha^{[A]}\rangle$ and $|\Phi_\alpha^{[B]}\rangle$ are eigenvectors of the reduced density matrices $\rho^{[A]}$ and $\rho^{[B]}$ with corresponding eigenvalues $|\lambda_\alpha|^2 > 0$. The coefficients λ_α satisfy the relation $\langle\Phi_\alpha^{[A]}|\Psi\rangle = \lambda_\alpha|\Phi_\alpha^{[B]}\rangle$. Here χ_α is the *rank* of the decomposition and it is a natural measurement of the entanglement between the two partites A and B.

The entanglement is quantified by $\chi = \max_A \chi_A$ over different bipartite decompositions. The focus is on systems which are weakly entangled and χ may grow as fast as a polynomial of degree N. The entanglement is at maximum when a half of the qubits is in partite A and the other half of the qubits is in B, and the upper limit is bounded by $2^{n/2}$. Also during the time-evolution of the system the entanglement remains small and has a upper bound of the order of a polynomial degree n. These systems belong to the class of *slightly entangled* systems. By a consecutive application of SD on each partite, the coefficients $c_{i_1,\ldots,i_N}$ can be written in terms of N tensors $\{\Gamma^{[1]},\ldots,\Gamma^{[N]}\}$ and $(n-1)$ vectors $\{\lambda^{[1]},\ldots,\lambda^{[2]}\}$ [40]. The coefficients rewritten in terms of Γ and λ are given as follows:

$$c_{i_1,\ldots,i_N} = \sum_{\alpha_1,\ldots,\alpha_{N-1}} \Gamma_{\alpha_1}^{[1]i_1}\lambda_{\alpha_1}^{[1]}\Gamma_{\alpha_1\alpha_2}^{[2]i_2}\lambda_{\alpha_2}^{[2]}\ldots\Gamma_{\alpha_{N-1}}^{[N-1]i_{N-1}}. \tag{A.8}$$

Now the 2^N coefficients $c_{i_1,\ldots,i_N}$ can be expressed by $2(N-2)\chi^2+(N+3)\chi$ parameters. This decomposition is commonly known as the *Vidal decomposition* [137].

To interpret the A-matrices in Eq. (A.4) in terms of the Vidal decomposition, let us introduce the Kronecker delta with a dummy primed index and rewrite:

$$\Gamma_{\alpha_{n-1}\alpha_n}^{[n]i_n}\lambda_{\alpha_n}^{[n]}\Gamma_{\alpha_n\alpha_{n+1}}^{[n+1]i_{n+1}} = \sum_{\alpha_n'} \Gamma_{\alpha_{n-1}\alpha_n}^{[n]i_n}\lambda_{\alpha_n'}^{[n]}\delta_{\alpha_n\alpha_n'}\Gamma_{\alpha_n'\alpha_{n+1}}^{[n+1]i_{n+1}}. \tag{A.9}$$

The vector $\lambda^{[n]}$ and the Kronecker delta define a new diagonal matrix $\Lambda_{\alpha_n\alpha_n'}^{[n]} \equiv \delta_{\alpha_n\alpha_n'}\lambda_{\alpha_n'}$. Hence, the Eq. (A.8) is rewritten as follows:

$$c_{i_1,\ldots,i_N} = \sum_{\alpha_1,\ldots,\alpha_{N-1}} \sum_{\alpha'_1,\ldots,\alpha'_{N-1}} \Gamma^{[1]i_1}_{\alpha_0\alpha_1} \Lambda^{[1]}_{\alpha_1\alpha'_1} \Gamma^{[2]i_2}_{\alpha'_1\alpha_2} \Lambda^{[2]}_{\alpha_2\alpha'_2} \Gamma^{[3]i_3}_{\alpha'_2\alpha_3} \ldots \Gamma^{[N-1]i_{N-1}}_{\alpha'_{N-2}\alpha_{N-1}} \Lambda^{[N-1]}_{\alpha_{N-1}\alpha'_{N-1}} \Gamma^{[N]i_n}_{\alpha'_{N-1}\alpha_N}, \tag{A.10}$$

and the summation over the common indices (matrix multiplication) between $\Gamma^{[n]}$ and $\Lambda^{[n]}$ yields

$$c_{i_1,\ldots i_N} = \sum_{\alpha'_1,\ldots,\alpha'_{N-1}} A^{[1]i_1}_{\alpha_0\alpha'_1} A^{[2]i_2}_{\alpha'_1\alpha'_2} \ldots A^{[N-1]i_{N-1}}_{\alpha'_{N-2}\alpha'_{N-1}} A^{[N]i_N}_{\alpha'_{N-1}\alpha_N}, \tag{A.11}$$

where substitutions are made according to

$$A^{[n]} = \begin{cases} \Gamma^{[N]}, & \text{if } n = N \\ \sum_{\alpha_n} \Gamma^{[n]} \Lambda^{[n]}, & \text{otherwise.} \end{cases} \tag{A.12}$$

We take another step further by summing over the primed indices, so that the original MPS representation (A.4) is achieved:

$$c_{i_1,\ldots,i_N} = A^{[1]}_{i_1} A^{[2]}_{i_2} \ldots A^{[N-1]}_{i_{N-1}} A^{[N]}_{i_N} \tag{A.13a}$$

$$|\Psi\rangle = \sum_{i_1,\ldots,i_N} A^{[1]}_{i_1} A^{[2]}_{i_2} \ldots A^{[N-1]}_{i_{N-1}} A^{[N]}_{i_N} |i_1 i_2 \ldots i_N\rangle. \tag{A.13b}$$

The Schmidt decomposition is essentially a singular value decomposition. It can be clearly seen that λ's are the singular values of SVD and Γ's are unitary matrices of the decomposition.

The most important advantage of such a representation is the fact that the speed of the computation would drastically increase since it is obvious from the representation that the multiplication of the matrices can be carried out in a parallel fashion. Yet another advantage of this method is that the small singular values could be neglected and only the essential part of the information can be kept by removing them. This could save a considerable amount of memory in the computation. Not surprisingly, SVD is widely used in image and audio compression such as in JPEG and MP3 file formats. The method is exactly the same as removing the non-essential singular values of the matrix representing graphical data [138].

Also the present method could be fully integrated with the variational method in order to optimise the interaction of the system with an external agent (*ancilla*). Ancilla systems are external agents which couple the qubits through some specific interaction in order to introduce entanglement between the qubits. This interaction could be especially the Heisenberg interaction (exchange interaction between spins). It has been shown that a universal quantum gate for a universal quantum computation can be constructed by the means of the Heisenberg interaction [139]).

After the interaction of the ancill, it decouples from the system and the system is found in an entangled state. But this condition is an ideal one and thus one cannot expect that the ancilla system necessarily decouples from the qubits. Hence, an optimised procedure must be used to minimise the distortion of the system meanwhile produce the necessary entanglement required for the computation [132, 140].

In this thesis we have considered only one-electron QCA, but for the next step with QCA consisting of many electrons, we could potentially use the MPS representation. One has to bear in mind that the MPS method is only applicable to one-dimensional systems such as a one-dimensional array of spins or atoms, or as in this thesis, a chain of QDs. The extent of the formalism to a general case in which the sub-systems form a network is known as the *projected entangled pair state* [141–143].